Morphology Optimization and Photophysical Properties of Methylammonium Lead Triiodide (MAPbI$_3$) Thin Films

MSc. Thesis submitted to

Zernike Institute for Advanced Materials

Faculty of Mathematics and Natural Sciences

University of Groningen

By

SAMPSON ADJOKATSE

Top Master in Nanoscience
(S2300664)
August 2014

Supervisor:

Prof. dr. M.A. Loi

Photophysics and OptoElectronics Unit

Referent:

Prof. dr. T.T.M. Palstra

Solid State for Materials Electronics

ABSTRACT

Recently, organic-inorganic halide perovskite materials have become pre-eminent in photovoltaic technology because of the high light-harvesting capabilities demonstrated in perovskites such as methylammonium lead halides, $MAPbX_3$ (X = Cl, Br, I). These perovskite absorbers are prepared from low-cost and abundantly available components, which may allow cheap photovoltaic devices fabrication. Although the first perovskite-sensitized solar cell was reported only in mid-2009, having power conversion efficiency of 3.8%, the past four years have seen an unprecedented rapid progress with energy conversion efficiencies reaching 17.9% at the end of 2013 and unconfirmed values as high as 19.3% have been recently claimed. Nonetheless, several pressing open questions remain, among which include their morphology, the nature of the fundamental optical excitations, charge transfer dynamics etc.

In this thesis, the morphology optimization and characterization of $MAPbI_3$ thin films and the photophysical investigations of their intrinsic properties are reported. The thin film deposition is optimized using single-step precursor deposition or the inter-diffusion reaction method; based on spin-coating and doctor blading deposition techniques. The latest gave rise to a relatively good control of the film uniformity and reproducibility. Temperature dependent steady-state and time-resolved PL measurements in the 5–293 K interval show a single emission peak around 780 nm at room temperature. However, two intriguing emission peaks appeared at ~ 745 nm and ~ 795 nm when the temperature is lowered from 150 K and remained till 30 K where only one peak is observed at ~ 780 K. Power dependent PL measurements show a gradual blue-shift of the emission peak with increasing power intensity while the transient PL measurements show an extreme increase in decay time from 83.7 ns to 6960 ns at 293 K and 50 K respectively with a small decrease to 4704 ns at 5 K.

ACKNOWLEDGEMENTS

Table of Contents

CHAPTER 1

INTRODUCTION

Concerns about environmental pollution, exhaustion of fossil fuels and increasing global crisis have accelerated the search for clean and cheaper renewable energy sources in the past decades. Arguably, the most abundant clean source of sustainable energy that is capable of yielding sustainable economic growth with minimum detrimental impact on the environment is sunlight. Nevertheless, the challenge in harnessing this energy is the development of low cost, efficient and stable photovoltaic (PV) devices. The two major state of the art PV technologies are the crystalline silicon and organic photovoltaic (OPV) technologies.

Commercially available crystalline silicon-based technology is characterized by power conversion efficiencies (PCE's) as high as 25% under standard testing conditions, has high carrier mobilities and high robustness. However, there are significant drawbacks such as high cost of production resulting in long payback time, high silicon purity requirements, high fragility and bulkiness of devices. On the other hand, the organic photovoltaic devices have their photoactive layer made from conjugated polymers which have high absorption coefficient, requiring only a thin layer to absorb most of the incident light. They are also generally soluble in organic solvents and exhibit many advantages including ease of production, lightweight, flexibility and semi-transparency. Nevertheless, OPV devices have low efficiencies (~ 11%) as a result of inefficient charge separation of electron-hole pairs and low carrier mobilities and also, have low stability due to chemical reactions with water and oxygen. Besides the commercially available crystalline silicon-based solar cells, which continue to advance in efficiency and reduce in cost of fabrication over the past four decades [1], there are many other newer solar cell technologies that promise lower cost solar power. One of such emerging PV technologies, which promise to be a serious contender for utility-scale solar power is the solution-processed hybrid organic-inorganic perovskite-based solar cell technology [2-10].

Perovskite materials constitute a very important niche within materials science displaying a multitude of properties including insulating, antiferromagnetic, piezoelectric, thermoelectric, semiconducting, conducting, colossal magnetoresistance, ferroelectricity, superconducting etc. [11,12]. They are a class of materials that adopt the same crystal structure as calcium titanate ($CaTiO_3$) with the generic formula, ABX_3 where the A and B sites usually accommodate inorganic cations of various valency and ionic radius and the X site accommodates anions (halogen or oxygen). By replacing the A cations with suitable

organic species, a sub-family of hybrid organic-inorganic perovskite is created [11]. This hybrid combines the advantageous properties that characterize crystalline inorganic solids with those of the organic molecules.
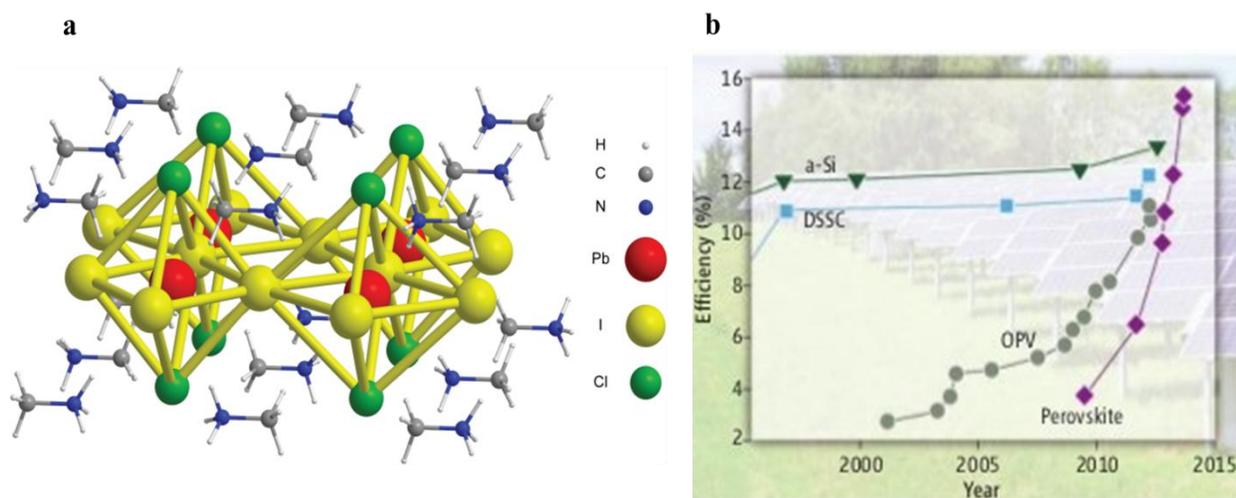
Figure 1.1. (a) Possible crystal structure of the hybrid perovskite $CH_3NH_3PbI_{3-x}Cl_x$ [16]. (b) Comparison of the rate of increase in perovskite solar cell efficiencies with leading second generation solar cells: amorphous silicon (a-Si), dye-sensitized (DSSC) and organic (OPV). Adapted from [13]

Hybrid organic-inorganic halide perovskite materials have attracted much attention recently due to the impressive high efficiencies recorded in perovskite-based photovoltaic over a very short period since the seminal work of T. Miyasaka and co-workers in 2009 [3]. The crystal structure of these materials is composed of an octahedral coordinated lead (Pb) atom with corner-sharing halogens and A-site organic ligands [Figure 1.1(a)]. Presently, the crystallographic data on the precise orientation of the organic ligands are not known. Figure1.1 (b) shows the comparison of the impressive rate of increase in the perovskite-sensitized solar cell (PSSC) efficiencies with leading second-generation solar cells: amorphous-silicon (a-Si), dye-sensitized solar cells (DSSCs) and organic photovoltaic (OPV). Perovskite-sensitized solar cells have emerged from the field of dye-sensitized solar cells (DSSCs) [14]. This emergence was motivated by the quest to find more advanced materials which absorbs strongly over a broader range than conventional dyes and also combines good optical absorption characteristics with efficient charge-transport properties. The first perovskite-sensitized solar cell was reported by T. Miyasaka's research group and had power conversion efficiency (PCE) of 3.8%, employing mesoporous TiO_2 sensitized with methylammonium lead triiodide ($MAPbI_3$) absorber and filled with iodide/triiodide redox couple [3]. Later, Park's research group optimized the titania surface and the perovskite processing and recorded more than double efficiency (6.5%) in liquid electrolyte-based $MAPbI_3$-sensitized solar cell

[8]. Subsequently, solid-state perovskite-sensitized solar cells were developed employing organic p-type hole conductor, namely 2,2′,7,7′-tetrakis-(N,N-di-p-methoxyphenylamine)9,9′-spirofluorene (Spiro-OMeTAD) as a hole transporter and methylammonium lead iodide chloride ($MAPbI_{3-x}Cl_x$) perovskite or $MAPbI_3$. These devices yielded between 8 and 10% maximum sun power conversion efficiencies respectively [2, 4].
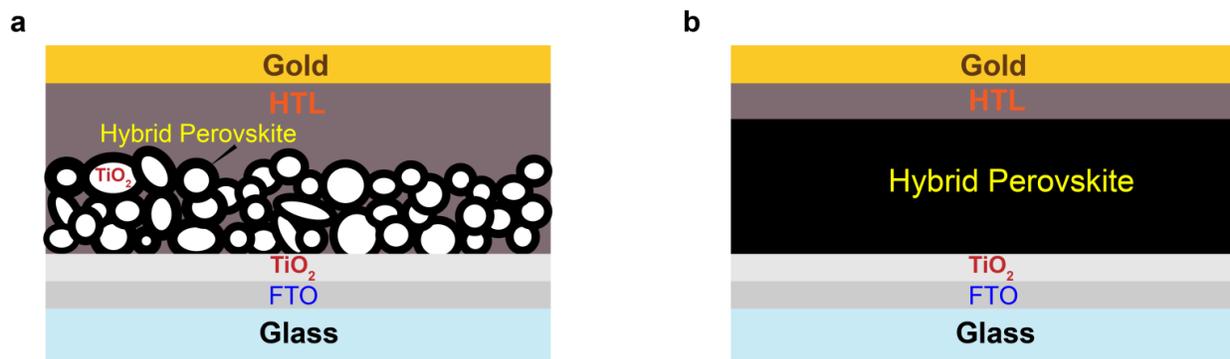
Figure 1.2. Two device architectures of hybrid perovskite solar cells. (a) Hybrid perovskite solar cell on mesoporous TiO_2, (b) Planar hybrid heterojunction perovskite solar cell. [16]

The impressive power conversion efficiencies recorded based on the hybrid halide perovskite materials and the drive to achieve lower cost and higher efficiencies has resulted in various device architecture modifications, two of which are shown in Figure 1.2. This has led to the replacement of the original DSSC geometry with the mesoporous TiO_2 with other simpler device structures. For example, in the studies of Kim *et al.* [4] and Heo *et al.* [15], the thin perovskite layer was sandwiched between an n-type mesoporous TiO_2 photoanode and a p-type hole transporting layer such as Spiro-OMeTAD. Lee *et al.*, replaced the electron-accepting mesoporous TiO_2 with insulating Al_2O_3, which acts as a scaffold instead of an electron-accepting layer and recorded faster charge transport, implying a good electron transport property of the perovskite and obtaining 10.9% efficiency. They also measured an increase in the open-circuit voltage (Voc) by 200 to 300 meV [2]. Etgar *et al.*, have also demonstrated good hole-transport properties in a simple two-component TiO_2-$MAPbI_3$ solar cell with 5.5% efficiency but lower Voc [9]. These studies indicate the ambipolar charge transport capabilities of $MAPbI_3$ and other hybrid perovskite materials studied [6]. Thus, perovskite materials have the capabilities of not serving only as a light harvester but also as a charge-carrier transporter.

Since the middle of 2013, several milestones in PCE improvement are being witnessed due to the innovation of the cell fabrication technique, which leads the efficiency of organometal halide perovskite based solar cells over 15%. The introduction of an inter-diffusion reaction (sequential deposition) method

for the fabrication of perovskite on the mesoporous-TiO_2 film gave a PCE of 15% and a certified value of 14.1% [17]. Also, planar heterojunction perovskite solar cell fabricated by vapor deposition demonstrated 15.4% PCE which matched the 15% efficiency record of the mesoporous cell [18]. Besides these, a series of eye catching PCE values were reported: 15.6% [19], 15.7% [7] and 15.9% [20] and by the end of 2013, 17.9% [21] efficiency was certified with unconfirmed values as high as 19.3% have been claimed [22].

To understand the fundamental photophysical mechanisms underlying the remarkable performance of these materials, independent investigations by Snaith's research group [23] and Nripan Mathews and collaborators [24] on the dynamics of the photoexcited species showed that the electron-hole diffusion lengths in solution-processed $MAPbI_3$ exceeds 100 nm. Snaith and co-workers also measured values of the diffusion length exceeding $1\mu m$ for the $MAPbI_{3-x}Cl_x$ mixed halide perovskite, an order of magnitude greater than the already remarkably high value of 100 nm for the pure iodide. Hence, giving that one of the bottleneck for low efficiencies in low-temperature solution-processed photovoltaic is poor exciton or electron-hole diffusion lengths which are typically about 10 nm, this high values measured in the hybrid perovskites heightens the hope to push the efficiency toward that of thin-film copper indium gallium selenide (CIGS) cells (PCE of 20.4%) and then toward and beyond that of single crystalline silicon devices (PCE of 25%).

Current perovskite absorbers producing these remarkable high efficiencies have band gap energy around 1.55 eV (corresponding to photon absorption at 800 nm) and photovoltage of 1.1 V as reported by Snaith's group [2]. This imply that the energy loss which is 0.45 eV, may be due to recombination, electron injection or hole extraction or both, in which case, the loss by electron injection or hole extraction is about 0.23 eV. If the perovskite material acts as not only a light harvesting material but also as an electron (hole)-transporting material, then the photovoltage will be determined (apart from about 0.3 – 0.35 V losses) by the difference between the Fermi energy of the perovskite material and the valence (conduction) band energy of the hole (electron)-transporting material. Thus, a perovskite layer that acts as both light harvester and ambipolar charge-carrier transporter can potentially achieve photovoltage exceeding 1.1V. Similarly, further improvement in the quality of the active material with higher mobilities can result in fill factors (FF) exceeding 0.7.

In spite of the steep increase of the power conversion efficiency in perovskite-sensitized photovoltaic devices over a very short period from April 2009 to date, where the beginning PCE of 3.8% has rapidly improved to 19.3%, this technology is still suboptimal. Among the diverse limitations such as light reflection by the substrates (transparent conducting oxides, glass, quartz, etc.) and the lack of better charge transporting layers, the main limitation to optimal performance is due to the large-scale

inhomogeneity (and reproducibility) in film uniformity and layer thicknesses. Figure 1.3 gives the SEM of the morphology of pristine $MAPbI_3$ and $MAPbI_{3-x}Cl_x$ films on glass [23]. These images illustrate the inhomogeneous and incomplete coverage of the perovskite film as a result of uncontrolled crystallization of the perovskite, which produces large morphological variations. This limits the maximum capabilities of these materials or the prospects of their practical applications. In addition, the standard fluorine-doped tin oxide (FTO)/compact (c)-TiO_2 combination and the mesoporous-TiO_2 or the insulating Al_2O_3 scaffold require rather high temperatures above 450 ^{o}C for their sintering. On the other hand, the mechanisms underlying such exceptional performances are not clearly understood.
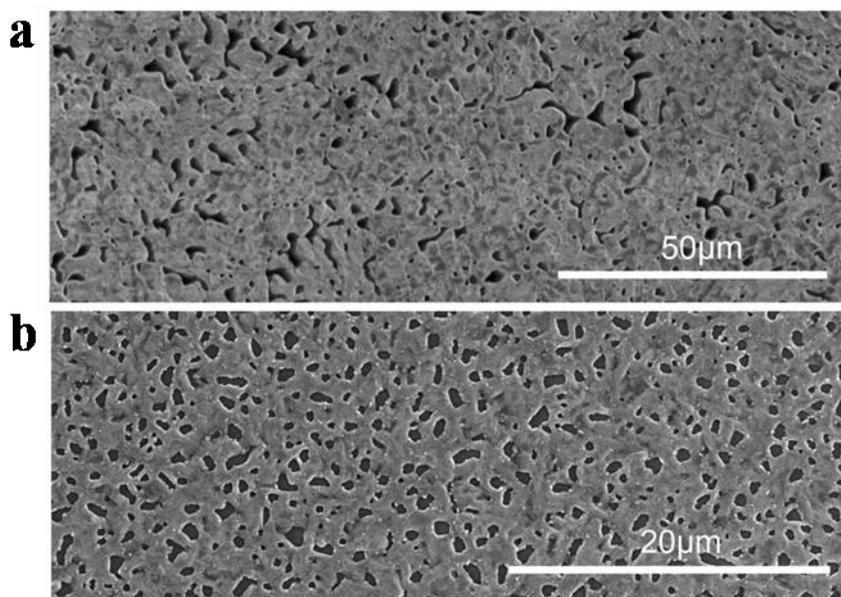
Figure 1.3. (a) Top view SEM of the morphology of a pristine $MAPbI_{3-x}Cl_x$ and (b) pristine $MAPbI_3$ films formed on glass [23].

In this study, our focus is on exploring methods to control the morphology of hybrid perovskite materials through better control of processing parameters and the photophysical investigation of the intrinsic properties of $MAPbI_3$ to understand the physical properties of this material. The standard FTO/c-TiO_2 combination will be replaced by indium tin oxide (ITO) as a transparent conducting oxide combined with or without a thin layer of aluminum-doped zinc oxide (AZO) which requires low processing temperatures of less than 150 ^{o}C.

Besides the literature review captured in the above introduction, the overview of this thesis is given as follows. The basic theory of solar cell devices and the photophysical mechanisms in semiconducting absorbers are presented in Chapter 2, expounding their working principles and limitations. While chapter

3 addresses the experimental methods and presents the various materials and methods used for the fabrication, Chapter 4 presents and discusses the experimental results. Finally, the summary is presented in Chapter 5.

CHAPTER 2

THEORY

2.1 Basics of Solar Cells

Understanding the basic driving mechanisms underlying solar cell operations in general is essential in improving solar cell efficiencies, stability and reducing cost. A solar cell is an electronic device which directly converts sunlight into electricity. Light shining on the solar cell produces both a current and a voltage to generate electric power. This process requires firstly, a material in which the absorption of light or photon with energy equal or greater than its bandgap excites an electron to a higher energy state, and secondly, the movement of this higher energy electron from the solar cell into an external circuit. The electron then dissipates its energy in the external circuit and returns to the solar cell. A variety of materials and processes can potentially satisfy the requirements for photovoltaic conversion but in practice nearly all photovoltaic energy conversion uses semiconductor materials in the form of a p-n junction. The p-n junction is composed of a p-doped and an n-doped layer on top of each other, creating a region at the interface called the depletion region or space charge region where very few mobile charge carriers reside. To date, many solar cells are built from thin films of inorganic, organic or hybrid semiconductors. The basic steps in the operation of a solar cell include the generation of light-generated carriers, the collection of the light-generated carriers to generate a current, generation of a large voltage across the solar cell and the dissipation of power in the load and in parasitic resistances [25].

In solar cells based on inorganic semiconductors, the absorbed photons are directly converted into free electron-hole pair or charge carriers (electron and hole) which are collected by the corresponding electrodes (anode and cathode). The electron-hole pair may be separated either by charge carrier drift driven by an externally applied voltage or by random diffusion towards the active area of the p-n junction where the pair is separated by the internal field of the depletion region. In organic photovoltaic devices, photoexcitation of a molecule leads to creation of a tightly bound electron-hole pair called an exciton. These electron-hole pairs are coulombically bound and can relax back to the ground state by multiple pathways. One of the pathways is the route in which charge carriers are created. The created excitons diffuse within the donor phase until they encounter the interface with the acceptor. Dissociation takes place via ultrafast charge transfer from the excited donor to the acceptor, leading to charge separation. Subsequently, photo-generated holes and electrons are transported through the donor and acceptor phases towards the electrodes with the aid of the internal electric field, caused by the use of electrodes with

different work functions. The photoactive (semiconducting) material is usually sandwiched between a high and low work function electrode, one transparent and the other reflecting.

As mentioned in the introductory chapter, hybrid solar cells are composed of crystalline inorganic and organic semiconductors, combining the advantageous properties of both components. The hybrid semiconductor may consist of a bilayer structure (junctions formed by two layers of distinct materials such as donor-acceptor heterojunction), bulk-heterojunction structure (active layer is composed of the blend of distinct materials of donor-acceptor combination) or a single polycrystalline layer such as in hybrid perovskites.

2.2 Solar cell characterization

The photovoltaic device's ability to convert the incident photon energy into electrical energy is determined by measuring its electrical current as a function of externally applied voltage both in dark and under illumination. This is referred to as the current-voltage (I-V) characteristics. However, it is more practical to plot the current density-voltage (J-V) characteristics which are normalized by the device active area since the power output of the device strongly depends on the size of the active area. A typical current-voltage characteristic of a solar cell in the dark and under illumination is displayed in Figure 2.1. In dark conditions, solar cells ideally operate as a diode and the current is given by the ideal Shockley diode equation:

$$J = J_0 \left[exp \frac{qV}{nkT} - 1 \right]$$

where J_0 is the saturation current density, n is an ideality factor and k is the Boltzmann constant. The curve shows negligible current in reverse bias and exponentially increasing current under forward bias conditions. Under illumination, an additional photocurrent J_{PH} contribution is added and the equation is modified to

$$J = J_0 \left[exp \frac{qV}{nkT} - 1 \right] - J_{PH}$$

leading to the downward shift of the entire curve as shown in Figure 2.1. The device produces power only in the fourth quadrant where the applied voltage is between zero and the open circuit voltage (V_{oc}). The V_{oc} is the maximum photovoltage that the device can produce under illumination and corresponds to the voltage where the current under illumination is zero. From the above equation, we find V_{oc} to be

$$V_{oc} = \frac{nkT}{q} \ln\left(\frac{J_{PH}}{J_0} + 1\right) \approx \frac{nkT}{q} \ln\left(\frac{J_{PH}}{J_0}\right)$$
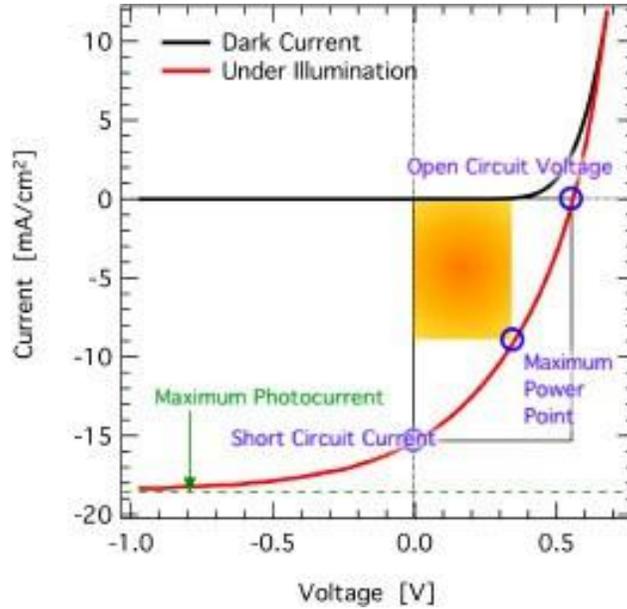
Figure 2.1. Typical current density-voltage characteristics of solar cell

In practice, the V_{oc} is affected by morphological features, non-ideal contacts and trap states formed at interfaces [26, 27]. Even though V_{oc} is largely independent of the work function of the electrode, it is solely dependent on the energetic and morphological structure of the active layer [28]. The maximum photocurrent the device can generate under illumination at zero potential difference between the anode and the cathode is the short circuit current density (J_{SC}). The short circuit current depends on the density of photons incident on the solar cell, the total absorbance of the device, the overlap of the absorption with the solar spectrum and the amount of charge carriers lost to recombination before extraction. J_{SC} represents the number of extractable photogenerated carriers. Another significant device parameter is the fill factor (FF) which is a measure of the quality of the current-voltage characteristics and is defined as the ratio of the maximum power point (P_{MPP}) and the product of J_{SC} and V_{OC}. The decrease in the fill factor is attributed to losses due to recombination. The FF is defined by:

$$FF = \frac{J_{MPP} \times V_{MPP}}{J_{SC} \times V_{OC}}$$

where V_{OC} and J_{SC} are the voltage and current density in the maximum power point respectively. The power conversion efficiency for a solar cell is also defined as:

$$\eta = \frac{P_{MPP}}{P_{in}} = \frac{J_{SC} \times V_{OC} \times FF}{P_{in}}$$

The strong interdependencies between the parameters in the numerator suggest that high efficiency can only be reached by joint optimization of V_{OC}, J_{SC} and FF. Similarly, the optimization of the device operation depends on several parameters such as morphology and thickness of the active layer, composition and size of the materials, temperature and light intensity.

2.3   Basic Mechanisms of Photoluminescence

Phenomena at surfaces and interfaces tend to dominate the behaviour of excitations in heterostructures, limiting the performance of many electronic and optoelectronic devices due to the nature of the heterojunction. Smooth and atomically abrupt interfaces are necessary for good optical and electrical reflection, and high carrier mobility. More importantly, defects and impurities provide new states for electrons and holes, altering their motion, lifetime and transition energies.
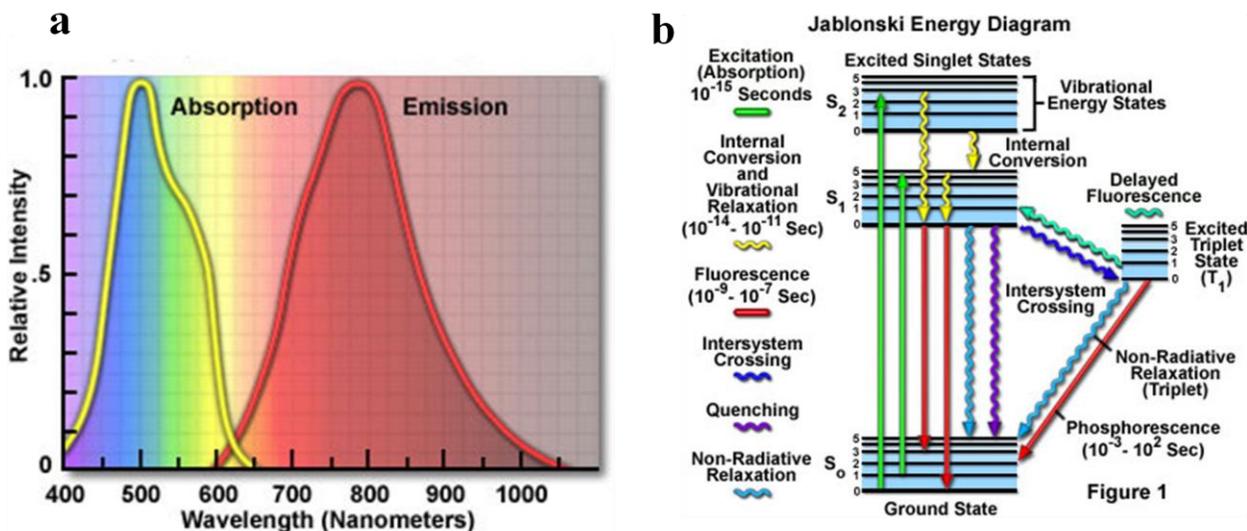

Figure 2.2. (a) Typical absorption and emission spectral profiles (b) Jablonski diagram showing basic photophysical processes; S denotes singlet, T triplet states.

When light of sufficient energy is incident on a material, photons are absorbed and electronic excitations are created. That is, the excitation promotes the molecule from its singlet ground state (S_0) to the first

excited singlet state (S_1). Eventually, these excitations relax and the electrons return to the ground state via radiative (recombination to the S_0 state giving rise to luminescence) or non-radiative transitions. If radiative relaxation occurs, the emitted light is called photoluminescence (PL). This light can be collected and analyzed to yield a wealth of information about the photoexcited material. The PL spectrum provides the transition energies, which can be used to determine electronic energy levels. The PL intensity gives a measure of the relative rates of radiative and non-radiative recombination. Variation of the PL intensity with external parameters like temperature and excitation power can be used to characterize further the underlying electronic states and bands. In Figure 2.2, the absorption and emission spectral profiles and the Jablonski diagram showing the basic photophysical processes are illustrated. The non-radiative processes competing with luminescence are energy loss to the local vibrations of surrounding atoms (called phonons in solids) and to electronic states of atoms in the vicinity, such as energy transfer, which may be resonant or phonon assisted.

The PL depends on the nature of optical excitation. The excitation energy selects the initial photoexcited state and governs the penetration depth of the incident light. The PL signal often depends on the density of the photoexcited electrons and the intensity of the incident beam can be adjusted to control this parameter. When the type or quality of material under investigation varies spatially, the PL signal will change with excitation position. In addition, pulsed optical excitation provides a powerful means for transient phenomena. Short laser pulses produce virtually instantaneous excited populations, after which the PL signal can be monitored to determine recombination rates.

Because PL often originates near the surface of a material, PL analysis is an important tool in the characterization of surfaces. The utility of PL for this purpose is derived from its unique sensitivity to discrete electronic states, many of which lie near surfaces and interfaces. Using the techniques noted above, the nature of these states can be probed in detail. The energy distribution and density of interface states can be ascertained by studying the excitation intensity dependence of the PL spectrum. The presence of surface adsorbates alters the intensity of the PL signal. When the states serve as long-lived traps, the depth of the trap can be determined by observing thermal activation in temperature-dependent PL. In fact, even if interface states are non-radiative, which is usually the case, the states alter the time-resolved PL of radiative transitions in the material. Non-radiative traps dominate the transient PL signal at low carrier density.

PL is simple, versatile, and nondestructive. The instrumentation that is required for ordinary PL work is modest: an optical source and an optical power meter or spectrophotometer. A typical PL set-up is shown in Figure 2.3. Because the measurement does not rely on electrical excitation or detection, sample

preparation is minimal. This feature makes PL particularly attractive for material systems having poor conductivity or undeveloped contact/junction technology. Measuring the continuous wave PL intensity and spectrum is quick and straightforward. On the other hand, investigating transient PL is more challenging, especially if recombination processes are fast.
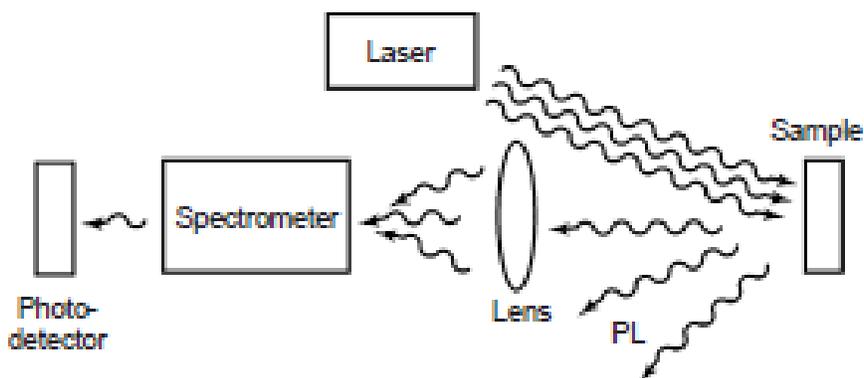
Figure 2.3. A schematic of a typical experimental set-up for PL measurements.

Because PL can be used to study virtually any surface in any environment, it can be used to monitor changes induced by surface modification in real time. For example, unlike most surface characterization techniques, PL is generally not sensitive to the pressure in the sample chamber. Hence, it can be used to study surface properties in relatively high-pressure semiconductor growth reactors. Although PL does depend quite strongly on temperature, liquid helium temperatures being required for the highest spectral resolution, room-temperature measurements are sufficient for many purposes. In addition, PL has little effect on the surface under investigation. Photo-induced changes and sample heating are possible, but low excitation can minimize these effects. In situ PL measurements do require optical access to the sample chamber. Yet, compared with other optical methods of characterization like reflection and absorption, PL is less stringent about beam alignment, surface flatness, and sample thickness.

The advantages of PL analysis listed above derive from the simplicity of optical measurements and the power to probe fundamental electronic properties. The chief drawback of PL analysis also follows from the reliance on optical techniques: the sample under investigation must emit light. Indirect-bandgap semiconductors, where the conduction band minimum is separated from the valence band maximum in momentum space, have inherently low PL efficiency. Non-radiative recombination tends to dominate the relaxation of excited populations in these materials. This problem can be augmented by poor surface quality, where rapid non-radiative events may occur. Nevertheless, once a PL signal is detected, it can be used to characterize both radiative and non-radiative mechanisms. Although it may not be possible to

identify directly the non-radiative traps via PL, their signature is evident in several types of PL measurements. Another shortcoming of PL is the difficulty in estimating the density of interface and impurity states. When these states have radiative levels, they are readily identified in the PL spectrum, and the size of the associated PL peaks provides a relative measure of their presence in the sample. However, measuring the absolute density of these states is a far more formidable task and typically requires an exhaustive analysis of the excitation intensity dependence of the PL signal.

CHAPTER 3

EXPERIMENTAL

3.1 Materials

As clearly stated, one of the aims of this study is to form an absorber-transport layer with homogeneous and continuous morphology in a structure that can later be used in solar cells. The samples and devices investigated are composed of one or more thin layers of absorber-transport layers built in a planar fashion on patterned indium tin oxide (ITO, or tin-doped indium oxide)-coated glass substrates. The properties and functions of the more relevant materials are discussed below. A collection of energy level alignments for different materials commonly used in perovskite based solar cells and in this study are shown Figure 3.1. It is very probable that at least some of these levels change, if brought into contact with each other. The band gaps and, even more important, band edge positions, reported in the literature are spread over a wide range.
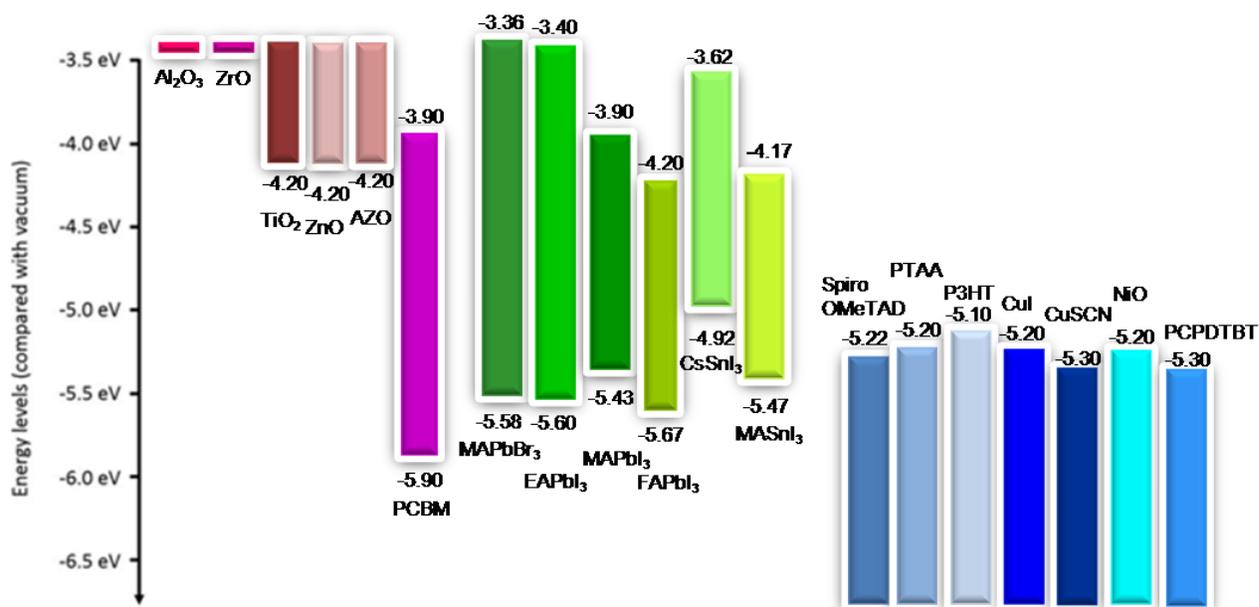

Figure 3.1. Schematic of literature values for energy level alignment for different materials acting as the electron selective contact material (ETM) (left), absorbers (middle) and hole selective contact materials (HTMs) (right) in solar cells.

3.1.1 ITO-coated Glass

Glass is an ideal substrate chiefly because of its flatness, rigidity and transparency in the visible and infrared spectrum, the spectral range of interest. Apart from providing a support that the oxides can grow on, it has the additional benefit of blocking most infrared wavelengths greater than 2 µm and converting it to heat in the glass layer. This helps to maintain a low temperature of the active layer or regions of the solar cell which degrades in performance as it heats up. Similarly, ITO is a premium transparent conductive oxide (TCO) having superior electrical conductivity and optical transparency, easy to deposit as thin film, stable and easy to pattern to form transparent circuitry or electrodes. ITO is a heavily doped n-type semiconductor and has a relatively high work function of ~ 4.8 eV which makes it suitable for use as an anode (hole-extracting electrode) [29]. Its high transparency and relatively high anti-reflective property allows it to be used as the front electrode for light trapping or capturing of light without shadow effects that limits device efficiency. Its high conductivity also allows efficient carrier transport. In addition, ITO thin films can operate under harsh environmental conditions of temperature and pressure; they have very high atmospheric stability. Furthermore, they are highly insoluble, allowing it to be used under solution/wet processing conditions such as cleaning in solvents and solution-processed deposition of other materials. The ITO-coated glass substrates used in this research are ready made by Philips Research Laboratory and requires minimal preparation before use.

3.1.2 AZO

Similar to ITO, aluminum-doped zinc oxide (ZnO:Al or simply, AZO) is a transparent conducting electrode material that can capture light into the active region as well as extract electron carriers. The constituents, Zn and Al are relatively common, much cheaper and less toxic compared to the generally used ITO. It has a work function of ~ 4.2 eV and optical bandgap of ~ 3.4 eV. Thus, it has a relatively good optical transmission performance and electrical conductivity (2.35×10^{-3} S/cm) in the near infrared and visible regions and can be used as a cathode material in inverted solar cell device architecture [30].

3.1.3 PCPDTBT

Poly[2,6-(4,4-bis-(2-ethylhexyl)-4H-cyclopenta[2,1-b;4-b']dithiophene)-alt-4,7-(2,1,3-benzothiadiazole)], simply known as PCPDTBT is a narrow band-gap semiconducting polymer which has an optical band-gap of approximately 1.7 eV. It has energy levels of -5.3 eV and -3.6 eV for the HOMO and LUMO respectively. The energy levels and molecular structure are depicted in Figure 3.1 and 3.2 respectively. It has the ability to inject holes and fill the pore-hole in the active layer to enhance the Voc and FF of the device.
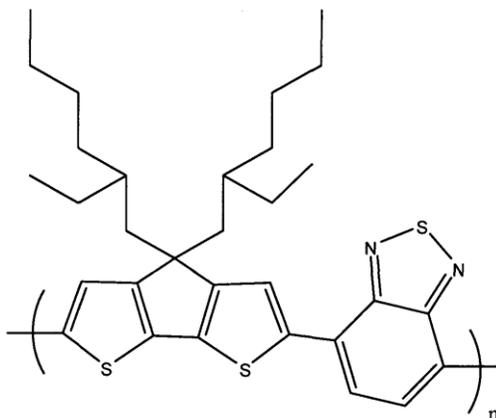
Figure 3.2. Molecular structure of the hole selective contact material (PCPDTBT) used in the device fabrication

3.1.4 Gold (Au) and Molybdenum trioxide (MoO₃)

With high stability and a work function of ~ 5.1 eV, Au is used as a back (anode) electrode in all the fabricated inverted devices in this study. It is a suitable hole extracting material. Similarly, molybdenum trioxide (MoO_3) is known to be one of the most interesting materials for stable hole selective contact because of its non-toxic nature and the very deep lying electronic states. MoO_3 is a high work function (~ 6.7 eV) transparent material which enhances performance when used as a window layer or hole transport buffer layer to improve the anode electrode efficiency in collecting and extracting positive carriers.

3.1.5 Organometal halide perovskite, CH₃NH₃PbI₃ (MAPbI₃)

The hybrid perovskite material of focus in this study is the semiconducting methylammonium lead triiodide ($MAPbI_3$), which serves as the active layer. The optical bandgap of this material is 1.5 eV and the energy level is at ~ 3.93 and ~ 5.43 eV. As mentioned in previous chapter, $MAPbI_3$ exhibits high optical absorption characteristics and has electron-hole diffusion length in excess of 100 nm. It is formed by either sequential deposition of precursor solutions of PbI_2 and MAI respectively or single-step deposition of the precursors in their right proportion and annealed at the optimal temperature (see later).

3.1.6 Solvent

Solution based deposition methods such as spin coating and blading coating were used in the fabrication processes. Depending on the solubility of the material, the processing parameters and the deposition methods, different organic solvents were used to dissolve the precursor materials. Some of the relevant solvents are briefly described below.

Chlorobenzene

This is an aromatic organic solvent that is colorless, flammable and has a high boiling point of 131 $^{\circ}$C. It provides a good solubility for a wide range of organic materials. In this study, it is used to dissolve PCPDTBT prior to device fabrication. Its slower evaporation rate enhances crystallinity of polymers.

2-propanol

2-propanol (isopropyl alcohol) is also a colorless liquid with a boiling point of 82.5 $^{\circ}$C. It is a non-polar solvent and beside its use as a cleaning fluid, it can be used to dissolve a wide range of non-polar compounds. It has a high evaporation rate and it's relatively non-toxic compared to other organic solvents. It is used to dissolve methylammonium iodide (MAI) prior to fabrication process.

N,N-Dimethylformamide

Like most organic solvents, N,N-Dimethylformamide (DMF) is a colorless liquid that is miscible with water and majority of organic liquids. It is a polar aprotic solvent with a high boiling point (153 $^{\circ}$C), thus, have low evaporation rate. It provides good solubility for organometallic compounds hence it's used in the synthesis of most of such compounds. The hybrid perovskite active layer and/or the PbI_2 precursor in this study are deposited from it.

3.2   CH$_3$NH$_3$I (MAI) Synthesis

Methylammonium iodide (CH$_3$NH$_3$I) was synthesized using the method described by Lee *et al*. [2]. Methylamine, 33 wt% in ethanol (Sigma-Aldrich) was reacted with hydroiodic acid (HI), 57 wt% in water (Sigma-Aldrich) at room temperature. The typical quantities were 24 mL methylamine, 10 mL hydroiodic acid and 100 mL ethanol. The HI was added drop-wise to excess methylamine in ethanol while stirring. After adding HI, the solution was stirred at room temperature for 2 hours before evaporating at 60 $^{\circ}$C. Crystallization of methylammonium iodide (MAI) was achieved after over 24 hours of continuous stirring and evaporation at 60 $^{\circ}$C, forming a white colored powder. The powder was washed using diethyl ether and dried in a vacuum oven at 60 $^{\circ}$C.

3.3   Thin Film and Solar Cell Fabrication

The fabrication of a thin film or device follows a series of processing steps and in a clean environment (cleanroom) where there is low level of environmental pollutants such as dust and grease. Minimal contamination, for instant by dust particles is essential since the samples or devices to be made are composed of thin films of a few to several nanometers and are less or comparable in thickness to dust

particle sizes which are typically of the order of ~1 µm. Thus, the presence of dust particles on a substrate or film can significantly affect the morphology of the film and thereby, affecting the performance of the device. In the extreme case, the pollutants can cause short circuit of the device. The different deposition methods and the details of the fabrication procedures are described below.

3.3.1 Deposition Methods

Deposition of thin films by spin coating method

This sample fabrication method is used to deposit uniform thin films on flat substrates and it involves casting a small amount of the solution of the coating material on the substrate (preferably at the centre) which is held in a holder (chuck). The substrate is then spun to the required rotational speed to spread and thin the fluid and eliminate excess material and solvents from the resulting film by centrifugal force. The quality and thickness of the thin-film formed on the substrate depends on the spinning parameters such as acceleration, spinning speed and spin duration as well as the concentration of the solution and the vapor pressure of the solvent. These parameters are varied in order to obtain an optimized film quality and thickness. It is important to note that the film thickness depends mainly on the concentration of the solution and the speed.

Deposition of thin films by blade coating (doctor blading) method

This technique is used for producing thin films on large areas. In this method, the solution of the material is casted directly at the edge of the main substrate or on a dummy substrate that is aligned in a row with the main substrate. The solution is deposited directly under the blade such that it spreads evenly across the width of the substrate. A constant relative motion is established between the blade and the stationary substrate to uniformly coat the material on the substrate to form thin film upon evaporation of the solvent. Several parameters can be controlled to influence the quality and thickness of the film. The thickness of the film largely depends on the speed of the blade and it increases with increasing speed, unlike in spin coating where the thickness is inversely proportional to speed. The concentration of the solution also affects the thickness. In this study, the main processing parameters considered for the deposition of the films are the concentration of the solution, volume of solution casted, blade height (slit), blade speed, pre-heated substrate temperature, time duration and temperature of annealing. All depositions were done in a nitrogen-filled glove-box environment.

Deposition of thin films by inter-diffusion reaction method

Inter-diffusion reaction method makes use of dip coating technique which involves the immersion of a pre-coated substrate into a container containing the solution of the coating material and allowing the material to apply itself to the substrate for an optimized time duration. The substrate is withdrawn after the coating, rinsed to remove excess material from the face of the film and dried. The film thickness is controlled by the coating viscosity and the withdrawal speed. This coating process can be done manually or automatically and in this study, the dipping was done manually to control the excess amount of the MAI. Thus, the substrate is immediately withdrawn after the conversion to the perovskite film (i.e. when the yellowish PbI_2-coated film changes to brown).

3.3.2 Fabrication Steps

Substrate Preparation

The first and foremost step in the sample preparation step is the substrate cleaning. A patterned ITO-coated glass, hereby referred to as the substrate with dimensions of 3×3 cm^2 is cleaned according to a well-tested procedure. In order to ensure smooth surface and to remove ITO-spikes that are capable of causing short circuit to the device or inhomogeneity in the film, each substrate was scrubbed manually with a warm ($50 - 70$ ^{o}C) solution of neutral soap and de-ionized (DI) water for about 5 minutes using plastic scrubbing gloves. The substrate was subsequently rinsed in a flow bath of DI water for 6-7 minutes. It was then sonicated twice each in DI water and acetone and once in isopropyl alcohol (IPA) respectively for 10 minutes in each case. Sonication in DI water and acetone help to remove dirt or soap on the ITO surface while the IPA is used to get rid of water and acetone. The substrates were either dried with a nitrogen gun or spin-dried before they are baked under ambient conditions in an oven at 140°C for 10 minutes to remove excess water and solvent. The final step involved UV-ozone treatment for 20 minutes. It is worth noting that during the cleaning and preparation procedures, the substrate is constantly kept in a class 1,000 air flow (ISO 7) to minimized contamination.

Solution Preparation

Preparation of solution is the next important step prior to fabrication. Depending on the solvent and the solubility of the materials, precursor solutions are prepared either on the same day or a day earlier. Generally, the required mass of the material is weighed on a scale with 0.1 mg precision and the appropriate amount of the required solvent added to achieve the desired concentration. The solution is stirred with a magnetic stir-bar either at room temperature (RT) or on a magnetic hotplate until the solute is sufficiently dissolved. The solutions are filtered using PTFE filters with varying pore sizes depending on the material, to extract aggregates or impurities that may be present in the solution. Solutions are

prepared either under ambient conditions or in a N_2-filled glove-box depending on the sensitivity, hygroscopicity or toxicity of the solvent or material.

In this project, several different concentrations and molar ratios for the MAPbI$_3$ thin film are examined. To form the MAPbI$_3$ precursor solution, methylammonium iodide and lead (II) iodide (Sigma Aldrich) are dissolved in anhydrous DMF at 1:1 or 3:1 molar ratios of MAI and PbI$_2$, with concentrations ranging from 150 mg/ml to 960 mg/ml. In the case of the inter-diffusion reaction (sequential deposition) of the inorganic and organic precursors, the PbI$_2$ precursor is dissolved in anhydrous DMF, making a 1M (~ 461 mg/mL) solution while the MAI precursor is dissolved in IPA at a concentration of 10 mg/mL. PCPDTBT is dissolved in chlorobenzene (CB) at concentrations of either 20 or 25 mg/mL and stirred overnight at ~ 65 ^{o}C. These solutions are stored under a nitrogen atmosphere.

Deposition of ETM

The hybrid perovskite material is deposited either directly on the cleaned ITO-coated glass substrate or on an electron transporting layer (ETM), making an inverted device structure. The commercially purchased AZO (ETM) suspension (2.5 wt.-% in isopropanol, 10 nm particle size) was obtained from Nanograde Llc. Before use, the solution is filtered with a 0.45 µm PTFE filter. The AZO dispersion is deposited via doctor blading without dilution at a blade speed of 5 mm/s. In order to control the film thickness, 60 µL of the AZO dispersion is deposited on the pre-heated substrate (30 ^{o}C) and annealed on a hotplate at 80 ^{o}C for 5 min.

Deposition of the active layer

The MAPbI$_3$ thin films are processed on glass/ITO or glass/ITO/AZO substrates either by single-step deposition of the MAPbI$_3$ precursor solution or by sequential deposition of the inorganic (PbI$_2$) and organic (CH$_3$NH$_3$I) precursor solutions via spin coating or doctor blading. With respect to single-step processing by spin coating, parameters which are varied include the spin-coating speed (1000 – 4000 rpm), spin-coating time duration (3 – 90 s), annealing temperature (RT – 100 ^{o}C) and annealing time duration (1 – 60 min). In the case of doctor blading, the main control parameters that are varied are blade speed (5 – 45 mm/s), pre-heated substrate temperature (RT – 100 ^{o}C), solution temperature (RT – 100 ^{o}C), annealing temperature (RT – 100 ^{o}C) and annealing time duration (5 – 30 min). Prior to the deposition, the substrates are kept at the pre-determined temperature for at least 5 min to ensure uniform substrate temperature is attained. On the other hand, the sequential deposition is done by first spin-coating or doctor blading the PbI$_2$ from DMF either on ITO or AZO and annealed at a pre-determined temperature (RT – 100 ^{o}C). Prior to immersing the PbI$_2$-coated film in the MAI solution, the PbI$_2$ film is

pre-wet in IPA for 1-2 sec and rinsed in IPA after the deposition for 2-5 min. The inter-diffusion reaction and annealing treatment of the films are carried out in a nitrogen-filled glove-box.

Deposition of the HTL

In order to fabricate a solar cell device with a hole transporting layer, PCPDTBT film is deposited from chlorobenzene on the glass/ITO/AZO/MAPbI$_3$ substrate that is kept at a pre-heated temperature (60 ^{o}C) via doctor blading by casting a 80 µL of the solution and at a blade speed of 5 mm/s. The sample is then annealed at 80 ^{o}C for 10 min. The deposition and annealing treatment of the films are carried out in a nitrogen-filled glove-box.

Thermal evaporation of top contact

To complete the solar cell device, a metallic anode consisting of 1 nm layer of MoO$_3$ followed by 100 nm of Au is thermally evaporated at 0.2 and 0.5 A/s respectively onto the active layer or the hole-transporting layer. This is performed to create an electrode (ITO) and counter electrode (MoO$_3$/Au) to obtain a circuit in which the electrons and holes can stream through the solar cell to obtain a current. This is done in a vacuum chamber (10^{-6} – 10^{-7} mBar) where the samples are suspended above a conductive boat containing small shards of the counter electrode material. A current is then fed through the boat, heating the counter electrode material until it evaporates upwards on the surface of the sample. A mask with four slots, one for each device area is used to ensure that the metallic electrodes are deposited to the ITO areas such that both electrodes are accessible.

3.4   Thin Film Characterization

Different characterization techniques are used to study and understand the morphological and photophysical properties of the hybrid perovskite material under study. In the following, the microscopy and spectroscopy methods in combination with other characterization methods used for the studies are briefly described.

Microscopy Measurement

The morphology of the active layer thin film is crucial to the performance of a solar cell device. Inhomogeneity and non-continuity as well as the presence of pin-holes and cracks in the active layer greatly affect device efficiency. In order to acquire qualitative information about the morphological properties of the layers, different microscopy tools are used. Atomic force microscopy (AFM) is a surface topography method that is able to obtain high-resolution surface topography images that reflects the material's surface properties. To acquire a topographical image, the sample is mounted on the scan

table/stage of the instrument. An AFM tip (some nanometer apex size) is set to slide on the surface of the film. Interaction forces between the tip and atoms of the sample surface (approximately nanonewton) cause a deflection of the lever on which the tip is mounted. Following a change of topography, a change in deflection of the lever occurs and a laser that hits the back side of the cantilever gets reflected towards a couple of photodiodes that adjust a ceramic piezoelectric to return the probe to its initial position. The recorded data is the voltage required to return the tip to its initial position. The interaction results in the formation of the images. With these images, fine details of the morphological properties of the materials are obtained. Two different equipment are used in the collection of the surface topography information: Multimode AFM NanoScope IV Scanning Probe Microscope Controller in tapping mode and AFM-SNOM (Scanning Near Field Optical Microscope) in contact mode. Besides AFM images, optical micrographs were also taken. Also, high-resolution optical images with depth selectivity were acquired using laser scanning confocal microscopy (LSCM) technique by using a Nikon Eclipse Ti inverted microscope system. This method has the capability to use its coherent light source (laser) to focus images at different depths below the surface of the film. All these analyses were performed in air.

Spectroscopy Measurement

Qualitative and quantitative information about the electronic structure and the dynamics of the photoexcited species are very significant to understanding the intrinsic properties of the photoexcitations. The information is obtained by interacting the material with electromagnetic fields. In this regard, absorption spectroscopy is used to measure the transitions between the electronic states and to obtain information about the absorptivity and band gap of the material. The absorption spectra are taken with UV/VIS/NIR spectrophotometer (Shimadzu UV-3600).

Another informative technique used to investigate the intrinsic properties of the perovskite samples is photoluminescence (PL) spectroscopy (steady-state and time-resolved PL). This information is acquired by exciting the sample with a short pulse of monochromatic light, followed by the measurement of the subsequent photoluminescence as a function of time. In this study, low-temperature steady-state and time-resolved PL measurements are performed on the samples at temperatures ranging from 5 K to 293 K. To cool the samples, they are loaded into a liquid helium cooled continuous flow (He-flux) Oxford Optistat cryostat. The samples are excited at ~ 400 nm by the second harmonic of a mode-locked Ti:Sapphire laser, tunable in the range ~720 – 980 nm, delivering pulses of 150 fs, with repetition frequency of ~76 MHz. To vary the repetition rate of the exciting pulse, an optical pulse selector is used. The Ti:Sapphire laser is pumped with a solid-state diode-pump, frequency-doubled Nd:Vanadate (Nd:YVO$_4$) laser, providing single-frequency green (532 nm) output at a power of 5 Watts. The steady

state PL spectrum is measured in the visible with a Hamamatsu EM-CCD camera. The time-resolved PL signal is recorded with Hamamatsu streak camera with a photocathode sensitive in the visible spectra range.

Thickness Measurement

The layer thickness measurement is taken using a Veeco Dektak 6M Profilometer which is accurate to ~5 nm. The layer thicknesses are extracted by calculating the height difference between the glass substrate and the top of the layer at different positions of the film and averaged.

J-V Characteristics

To acquire insight into the morphological effect of the active layer on device performance and the working mechanisms of the fabricated solar cells, current-voltage characteristics were measured using a Keithley 2400 SourceMeter in a nitrogen-filled glove-box. Measurements were made in the dark and under illumination from a Steurenagel SolarConstant 1200 metal halide lamp calibrated to 1 sun intensity (1 KW/m^2). The current-voltage characteristics were obtained in both forward and reverse biased conditions. To ensure a well-defined device area, the sample is covered with a device aperture mask with slightly smaller apertures than each of the respective device areas to eliminate current contributions from regions beyond the cathode/anode overlap. During measurement, the temperature (25 ^{o}C) is kept constant using a nitrogen flow.

CHAPTER 4

RESULTS AND DISCUSSION

4.1 Morphology Optimization and Characterization of $CH_3NH_3PbI_3$ Thin Films

As mentioned in the introduction chapter, the effective transfer of charge carriers requires a homogeneous and continuous structure of the active layer. This means that the morphology of the thin film of the active layer in a device is crucial to its performance. For instance, pinholes and cracks in the active layer greatly affect the performance of the device [23]. Thus, the degree of mixing of precursor materials, the size and composition of segmented domains, the crystalline character and the percolation pathways are all considered important in optimizing the photoactive layer. In this regard, the formation of hybrid perovskite from precursor solutions and the conditions under which they are formed are critical to the materials physical properties. Similarly, the presence and absolute amounts of the components (precursors) in the sample can affect its properties.

To date, perovskite films have been formed by versatile film deposition approaches. So far there have been four different deposition techniques reported for the fabrication of hybrid perovskite: single-step precursor solution deposition [4], inter-diffusion reaction (two-step sequential deposition) [17], dual-source vapor deposition [18] and vapor assisted solution process [31]. In this study, we employ the single-step and the two-step sequential deposition techniques based on spin-coating and doctor-blading methods to optimize the morphology of the active layer.

4.1.1 Morphology dependence on spin-coating deposition processes of the active layer

Much of the initial work of hybrid perovskite solar cells used spin-coating technique in depositing the active layer from single precursor solution due to its obvious simplicity [3]. Following this technique, the precursor solution of the perovskite was prepared by mixing stoichiometric quantities of CH_3NH_3I (MAI) and PbI_2 at 1:1 or non-stoichiometric 3:1 mole ratio in DMF or γ-butyrolactone (GBL) and stirred for several hours to get a clear solution. To reach optimized morphologies, several spin coating conditions or parameters were investigated including mole ratio of precursors, precursor solution concentration, the choice of solvent, spin coating speed and time duration, thermal annealing temperature and time duration.

First of all, attempts were made to optimize the thin film directly on ITO to make Schottky contacts. As mentioned earlier, different parameters were controlled. The thin films formed from the yellow precursor solution changes from yellow to brown upon annealing and are visually transparent. The brown colouration is an indication of the formation of the perovskite film. Qualitative analysis of the optical

microscope and AFM images of the thin films made from the equimolar precursor solution with 0.88 or 1 M concentration show fiber-like crystallites. These crystallites extend over long ranges and are randomly distributed. As the speed and time of spinning increases, the size of the fibers also increases. Generally, the films are inhomogeneous and non-continuous although there are films that exhibited homogeneity but are non-continuous and also of difficulty reproducibility. The concentration is noted to have a strong effect on the substrate coverage and on the crystal size. It was observed that as the concentration is lowered, the substrate coverage worsen but the fiber-like crystallites partially disappears even though the morphology is not improved. Figure 4.1a) shows an optical micrograph image of atypical morphology of MAPbI$_3$ thin film formed from 0.88 M equimolar solution in DMF on ITO-coated glass substrate. This film was spin coated at 1500 rpm for 3 sec and left to dry at room temperature (RT) for 30 min before annealing at 100 ^{o}C for 10 min. Even with variations in the deposition and post-deposition controlling parameters, all the films formed similar fiber-like crystallites. The observed features are likely due to excess of PbI$_2$in solution which normally crystallizes into needle-like crystals or as a result of non-favorable substrate surface chemistry. It may also be as a result of poor solubility of the precursors in the aprotic polar DMF solvent.
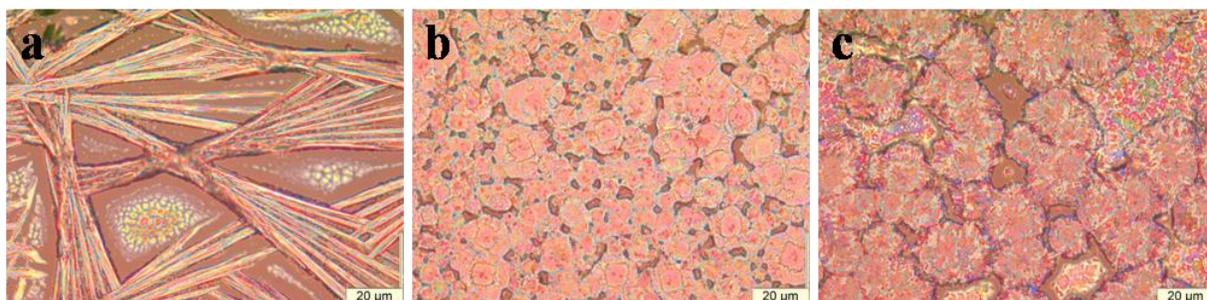

Figure 4.1. Optical micrographs showing the morphology of typical MAPbI$_3$ thin films deposited on ITO for different molar ratios of the precursors (MAI:PbI$_2$) in DMF or GBL. a) 0.88 M solution with 1:1 molar ratio of precursors in DMF b) 1 M solution with 3:1 molar ratio of precursors in DMF c) 1 M solution with 3:1 molar ratio of precursors in GBL.

In order to investigate the above conjectures, first of all, the proportion of the MAI component in the precursor solution was increased in order to form a 3:1(MAI : PbI$_2$) mole ratio solution at a concentration of 1 M instead of the equimolar composition. With this mole ratio solution, the morphology of the films was improved. However, although the films are still not perfectly homogeneous, there are no clear domains or fibre structures and the amount of pin-holes and cracks are significantly lower compared to those deposited from the equimolar solution. By lowering the crystallization rate via temperature ramping, a more homogeneous films were formed, but without complete elimination of the pores. The

number of pin-holes in the films reduced when the spin duration was increased from 5 to 30 s but degrades again for longer times. Similarly, when the films were deposited from GBL with the same 3:1 mole ratio of the precursors and concentration, similar patterns in morphology were observed but with larger grain sizes and less homogeneity. A quintessential morphology of the films deposited from DMF and GBL with the same parameters and conditions are illustrated in Figure 4.1 b) and c) respectively. These films were spin-coated at 1500 rpm for 30 s and allowed to slowly crystallize at RT for 20 min before annealing on a hotplate by ramping the temperature from room temperature (RT) to 100 ^{o}C at the rate of 5 ^{o}C/3min.The thicknesses of the films vary between 0.3 and 1 µm for speeds between 3000 and 1500 rpm and time durations between 30 and 5 s respectively.
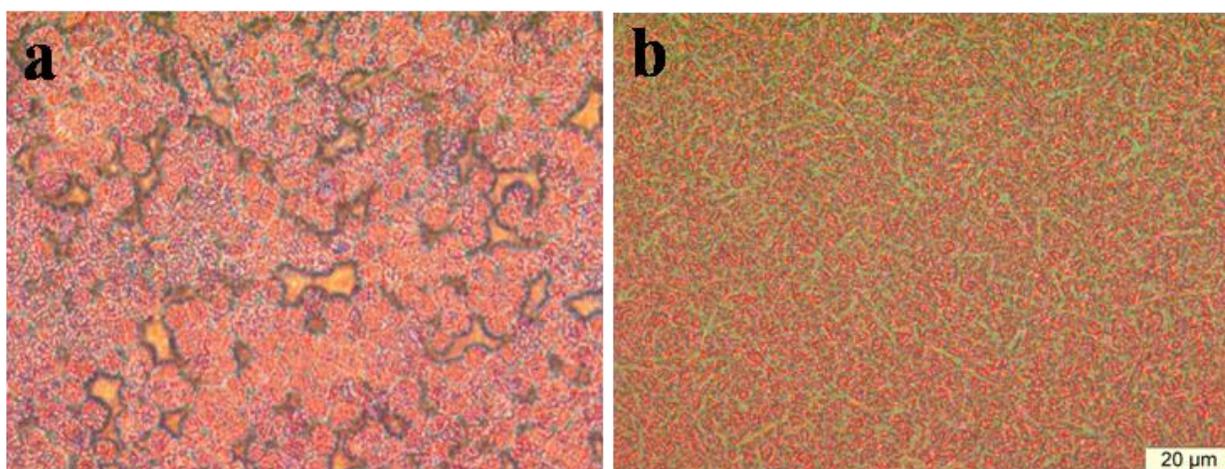

Figure 4.2. Optical micrographs showing the dependence of deposition technique on the morphology of MAPbI$_3$ thin film on AZO. (a) single-step deposition method (b) Inter-diffusion reaction method. a) has the same scale as b).

To test the effect of surface chemistry on the film morphology, the ITO-coated glass surface was modified with AZO of about 40 nm thickness. Beside surface modification, the AZO also serves as an electron transport layer. Single-step deposition of MAPbI$_3$ film from the 3:1 mole ratio precursor solution in DMF or GBL did not show significant influence on the film morphology or hole treatment. The perovskite poorly covers the AZO due to poor surface wetting. Figure 4.2a) shows optical micrographs of archetypal film morphology of the perovskite thin film fabricated via single-step precursor solution deposition under same conditions as on ITO.

Since no significant improvement in the morphology was obtained, an alternate deposition technique, the two-step sequential deposition method was employed. In this technique, the PbI$_2$ is first spin-coated from solution in DMF or GBL onto the ITO or AZO layer and subsequently transformed into the perovskite via

inter-diffusion by dipping into a solution of MAI in 2-isopropanol (IPA). Figure 4.2 b) shows the optical micrograph image of model MAPbI$_3$ film fabricated by this method on AZO layer. The PbI$_2$ film was spin-coated from a hot (70 $^{\circ}$C) solution of PbI$_2$ in DMF (1 M) at 4000 rpm for 90 s and annealed at 70 $^{\circ}$C for 20 min. It was subsequently dipped in MAI/IPA (10 mg/ml) solution for 90 s, rinsed in IPA for ~ 2 s before spin-drying at 2000 rpm for 20 s. It was finally annealed at 70 $^{\circ}$C for 20 min. Though the morphology of the perovskite film appears relatively homogeneous with fewer holes than in the one-step deposition method, the spin-coated PbI$_2$ films were highly non-uniform. Similar features were observed for the two-step sequential deposition on ITO substrates.

4.1.2   Morphology optimization based on doctor blading deposition

Analogous to morphology optimization by spin-coating processes, the MAPbI$_3$ films were also optimized by doctor blading method. As was described in chapter 3, materials deposition by blade coating enables film production on large areas and it's known to be an efficient technique for pore-filling in thin films. For this reason, the first endeavor was to make Schottky contacts similar to the spin-coating process. Both the one-step precursor solution deposition and the two-step sequential deposition methods were utilized. Film depositions by single-step procedure were made from the equimolar precursor solution in DMF at RT with 1 M concentration while for the sequential method, 1 M solution of PbI$_2$ in DMF and MAI/IPA (10 mg/ml) solution were used. The main coating parameters that were controlled or varied are blade coating speed, pre-heated substrate temperature and solution temperature.

The MAPbI$_3$ thin films deposited directly on ITO exhibited very different morphologies from those by spin-coating method. As shown in the model optical micrograph images of Fig. 4.3, the films are composed of domains with concentric layer morphologies. These films are blade coated from solution at RT and on substrates that were pre-heated at 100 $^{\circ}$C at coating speeds of 5, 10 and 15 mm/s, corresponding to Figure 4.3 a), b) and c) respectively and annealed at 100 $^{\circ}$C for 5 min. The images show the effect of blade coating speed on the shape and size distribution of the concentric domains. In this case, large domains that are randomly distributed and less substrate coverage are observed with increasing speed (film thickness). The films are also non-uniform with large pores. Also, in investigating the effect of pre-heated substrate temperature on the morphology, the temperature was varied between 50 and 100 $^{\circ}$C at the optimal coating speed of 5 mm/s. The concentric layer morphologies were reproduced and better substrate coverage was formed on the pre-heated substrate at 80 $^{\circ}$C as shown in the confocal micrograph image in Figure 4.4 a). Figure 4.4 b) and c) also show crystal size and substrate coverage distributions for temperatures at 90 and 100 $^{\circ}$C respectively. The crystallites are sparsely distributed with increasing temperature. The origin of the concentric layer morphology is not clearly known but can be attributed to

poor surface wetting which possibly leads to the formation of blobs on the surface which forms such morphology upon drying.
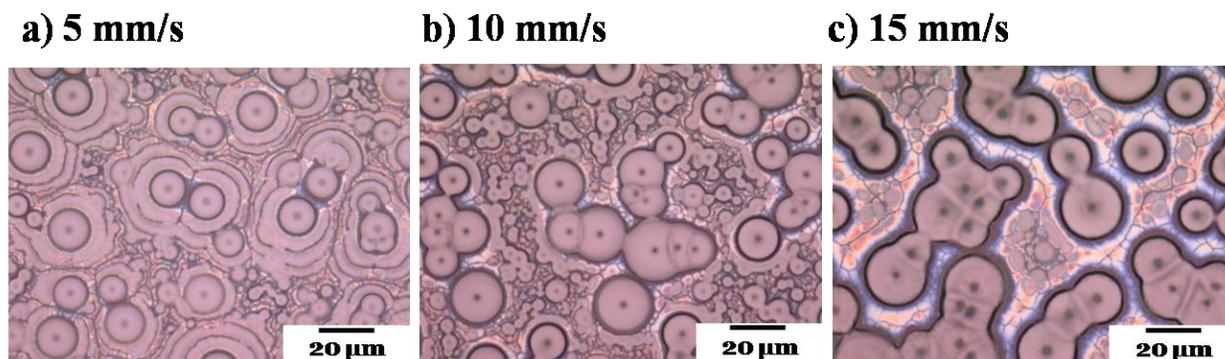

Figure 4.3. Model optical micrographs of MAPbI$_3$thin films deposited onpre-heated ITO at 100 ^{o}C and at blade coating speeds of 5, 10 and 15 mm/s corresponding to **a**, **b** and **c** respectively (i.e. increasing film thickness) and annealed at 100 ^{o}C for 5 min.


Figure 4.4. 100 µm × 100 µm confocal micrograph images of MAPbI$_3$thin films blade-coated on ITO at different pre-heated substrate temperatures of 80, 90 and 100 ^{o}C corresponding to **a)**, **b)** and **c)** respectively at 5 mm/s and annealed at 100 ^{o}C for 15 min.

Unlike the ITO/MAPbI$_3$ thin films, single-step deposition on AZO layer did not exhibit concentric layer morphologies; however, the films are segmented. The confocal micrographs in Figure 4.5 a) show the effect of coating speed on the film morphology. As shown in the figures, the quality of the films degenerate and the substrate coverage also decreases with increasing speed (film thickness). The better film quality is exhibited by the film fabricated at 5 mm/s, an observation which is consistent with the observed trend in the fabricated ITO/MAPbI$_3$ thin films. Hence, at this optimal speed, the pre-heated substrate temperature dependence of the film morphology was investigated for temperatures ranging between 50 and 100 ^{o}C. The fabricated samples were annealed at 100 ^{o}C for 15 min. From the confocal

micrograph images in Figure 4.5 b), it is observed that there is less substrate coverage and fibre-like crystallites formed at 50 °C. The crystallites gradually aggregate with improvement in the film quality as the pre-heated substrate temperature is increased. In particular, at the pre-heated substrate temperature of 100 °C, no fibre-like crystallites or crystal segmentation is observed over 50 μm lateral dimension. Microscopically, the film is homogeneous and continuous with very few pores. This implies that fast crystallization is required to form large domains with minimal pores and reduce roughness. In addition, high evaporation strongly improves film connectivity and substrate coverage on AZO thin films.
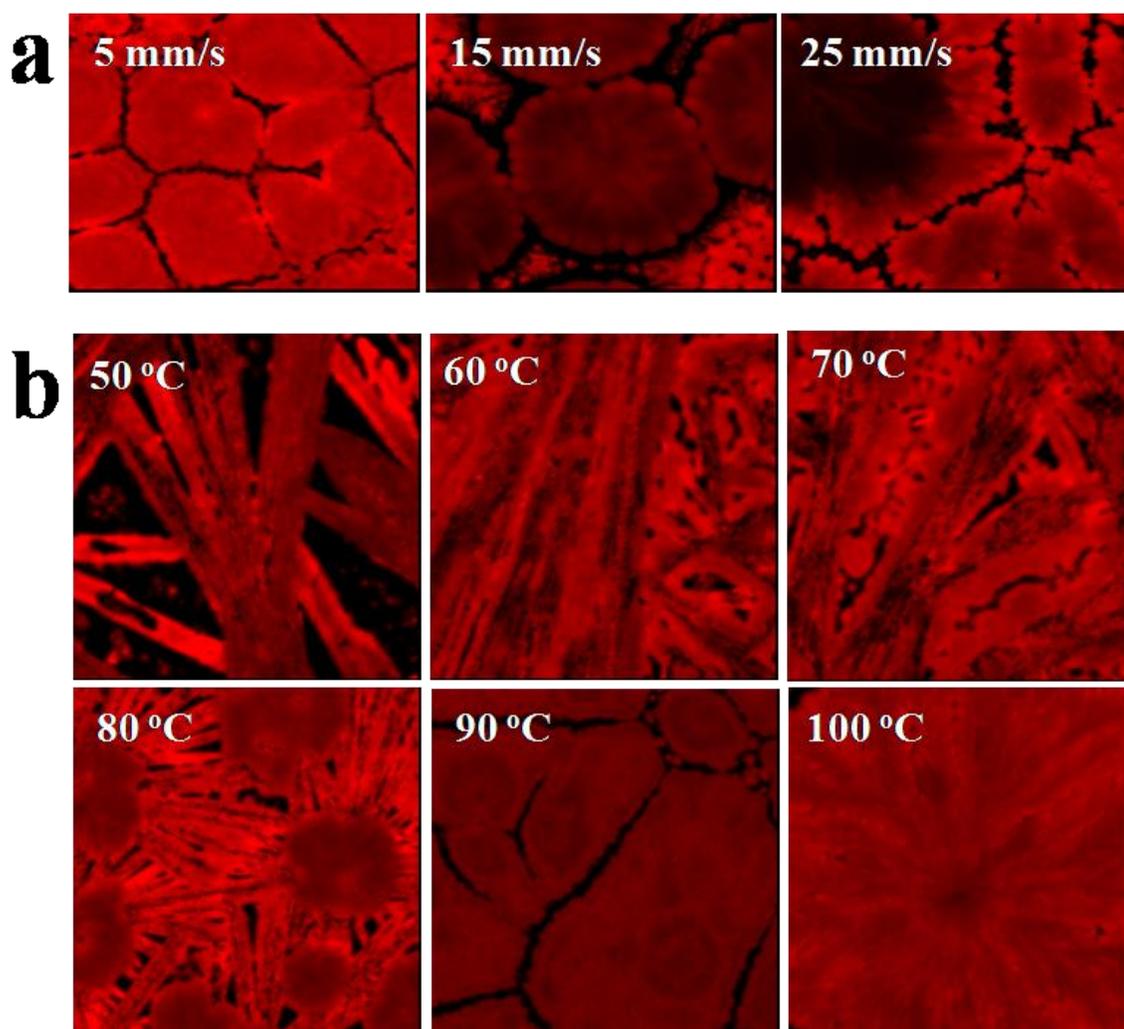

Figure 4.5. 50 μm × 50 μm confocal micrographs showing the blade speed and pre-heated substrate temperature dependence of the morphology of MAPbI$_3$ thin films deposited on AZO by single-step deposition method. a) Different blade coating speeds at a pre-heated substrate temperature of 80 °C. b) Different pre-heated substrate temperature. All samples were annealed at 100 °C for 15 min.

Figure 4.6.Optical micrographs of MAPbI$_3$ thin films deposited sequentially by dipping PbI$_2$ film that is blade coated under different conditions (of solution, substrate and annealing temperature) in MAI/IPA solution (10 mg/ml). The temperatures of the PbI$_2$ solution in DMF (1 M), substrate and annealing are respectively: a) 70, 50 and 70 ^{o}C b) 70, 80 and 70 ^{o}C (c) 100, 100 and80 ^{o}C. The coating speed and duration of annealing are 5mm/s and 30 min respectively for each.

Meanwhile, the inter-diffusion of MAI in solution into the blade coated PbI$_2$ thin films showed a very significant improvement in the quality of the film morphologies on the AZO layers. However, our studies reveal that the quality of the MAPbI$_3$thin film morphology is highly depended on the quality or thickness of the PbI$_2$ film which is also very sensitive to the pre-heated substrate temperature, solution temperature and coating speed. More importantly, we observed that fast evaporation or crystallization of the PbI$_2$ film results in continuous, homogeneous and highly transparent films. This suggests that film deposition on pre-heated substrates at higher temperature and at low speed are pre-requisites for optimal film morphologies. In Figure 4.6, the optical micrograph images show the dependence of pre-heated substrate temperature on the film quality of MAPbI$_3$ thin films. Though very little distinction is observed, the pre-coated PbI$_2$ films exhibited significant distinctions in the film quality at the different pre-heated substrate temperatures and at the coating speed of 5 mm/s. The quality of the films enhanced with increasing temperature. Speed or film thickness dependence effect on the quality of the PbI$_2$ coated films were also investigated at pre-heated substrate temperature of 100 ^{o}C and found that the morphology is highly thickness-dependent.

The optical micrograph images in Figure 4.7 a) reveal that the morphology of the PbI$_2$ film is optimal at a thickness of ~ 300 nm, below or above which the film degrades. Above the optimal film thickness, increasing growth of cracks is observed with increasing coating speed. The strong effect of the morphology of PbI$_2$ film on the MAPbI$_3$ thin film morphology is evident from Figure 4.7 b) and c) which shows the optical micrograph images and the corresponding AFM images respectively. Here we observe that the size of the crystallites, domains, holes and the surface roughness increase as the coating speed increases (decreases) above (below) the optimal speed (15 mm/s).
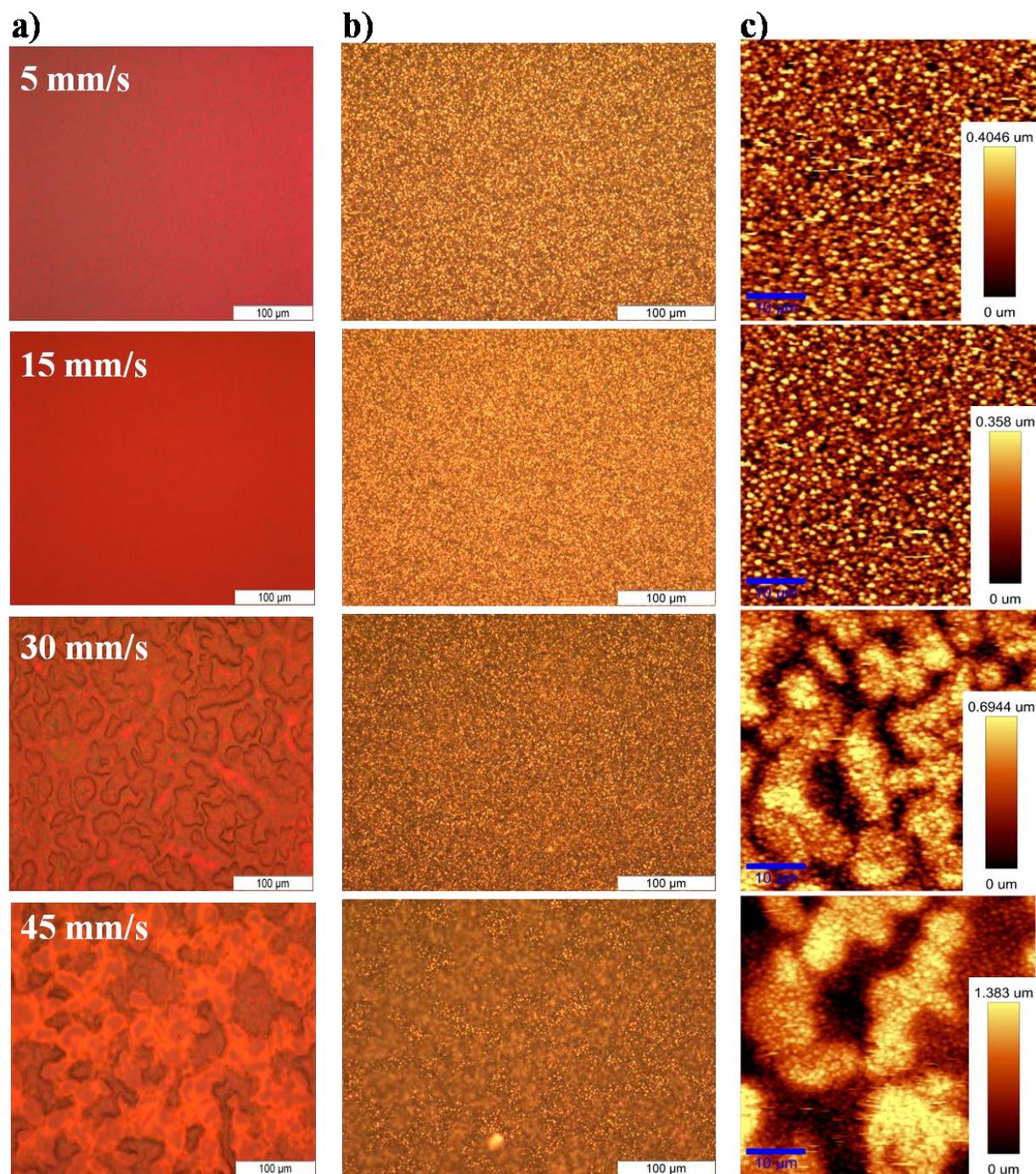
Figure 4.7. (a) Optical micrographs of PbI$_2$ films blade-coated on AZO at speeds of 5, 15, 30 and 45 mm/s respectively on a pre-heated substrate (100 ^{o}C) and annealed at 80 ^{o}C for 30 min (b,c) Corresponding optical micrograph and AFM images showing the morphology of MAPbI$_3$ thin films after inter-diffusion reaction of the PbI$_2$ coated films in MAI/IPA solution(10 mg/ml).

4.2 Morphology dependence of electrical properties: J-V Characteristics

The effect of film morphology on the device performance was investigated for the perovskite films deposited via single-step precursor solution deposition and two-step sequential deposition methods either with or without PCPDTBT as the hole transport material (HTM). MoO_3 was used as the buffer layer between the perovskite or HTM and Au electrode. Generally, the devices showed inferior performance and this is due to a number of factors including but not limited to bad morphology of the perovskite absorber and poor conductivity of the electron- or hole-selective contacts. In particular, majority of the devices fabricated via single-step precursor solution deposition method were completely shorted. On the other hand, deposition by the sequential method results in working devices even without the hole transport layer, except that the performances are inferior compared to reported efficiencies in literature. Figure 4.8 shows three characteristic J-V curves representing devices made by single-step deposition method with PCPDTBT layer, sequential deposition method without and with PCPDTBT layer, respectively corresponding to a, b and c in the figure. All coated layers were deposited by doctor blading method. Even though the poor device performances can be attributed to bad morphology, this is not entirely the case since reports from literature show high performances even with relative or worse morphologies of the active layer [32]. The method of absorber deposition is most likely to have had a great influence on the device performance. A possible reason for the extreme low efficiencies recorded can also be attributed to the absence of mesoporous electron transporting scaffolds for the $MAPbI_3$ absorber [23,18]. Nevertheless, it's important to mention that due to time limitation, only a limited number of devices were produced and the top layer was also not fully optimized. These results and the possible factors that affect device performances therefore allow for further investigations.
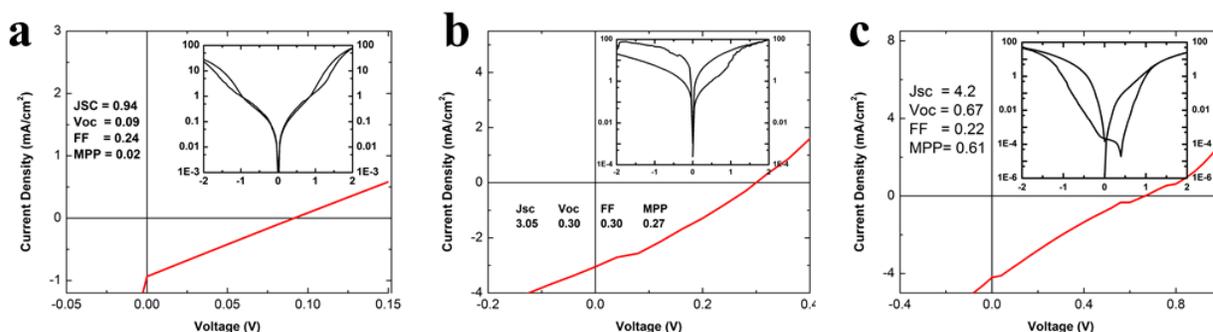

Figure 4.8. J-V curves for blade-coated devices. a)ITO / AZO / $MAPbI_3$ (2L) / PCPDTBT / MoO_3 (5nm)/Au (100 nm) by single-step deposition using 0.88 M equimolar solution. b) ITO/ AZO / $MAPbI_3$ / MoO_3 (1nm) / Au (100 nm) by two-step deposition of active layer. c) ITO / AZO / $MAPbI_3$ / PCPDTBT / MoO_3 (1nm) / Au (100 nm). (a) and (b) are by two-step deposition of active layer.

4.3   Photophysical Mechanisms in CH₃NH₃PbI₃ Thin Film

4.3.1   Absorption and photoluminescence of CH₃NH₃PbI₃ Thin Film

To ensure that the material under investigation is the MAPbI$_3$ absorber, absorption and steady-state photoluminescence measurements were taken. These measurements also provide information about the purity and quality of the material. The archetypal steady-state optical absorption and photoluminescence (PL) spectra of the MAPbI$_3$ thin film measured at room temperature are reported in Figure 4.9. The absorption spectra demonstrated good light harvesting capabilities over the visible to near-infrared spectrum with two distinct peaks located at ~480 and~760 nm in agreement with values reported in literature [2,4,6,8,9,15,17]. While the origin of the first absorption peak at 480 nm is not clearly known, the peak at 760 nm is ascribed to direct gap transition from the first valence band maximum to the conduction band minimum. This type of absorption spectra is observed in all the films fabricated. Also, the PL spectra of the thin film shows a relatively narrow band centered around 780 nm (~1.6 eV) with a small Stokes-shift. The narrow linewidth of the spectra is an indication of a relatively homogeneous thin film.
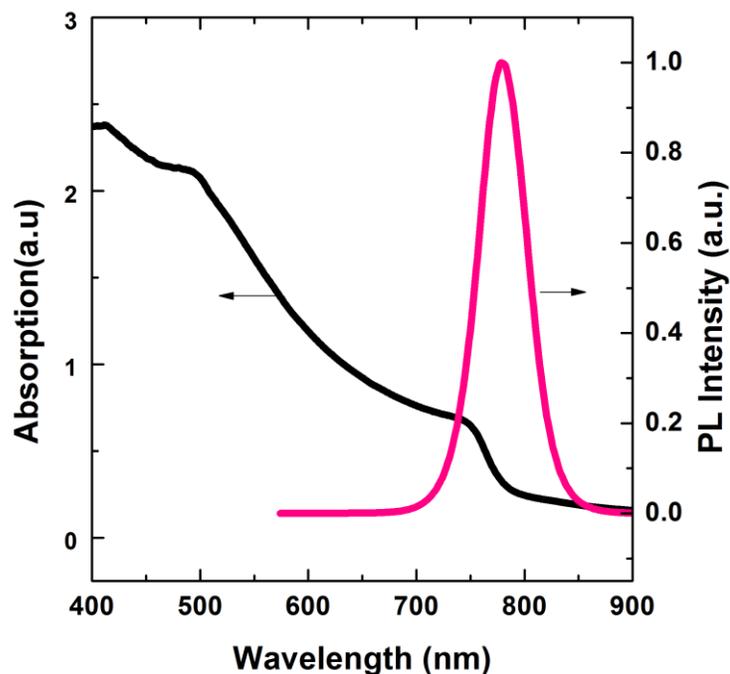

Figure 4.9. Absorption and steady state photoluminescence (PL) of CH₃NH₃PbI₃ thin film.

4.3.2 Temperature and power dependent steady state PL of MAPbI₃ Thin Film

Figure 4.10 shows the temperature dependence of steady state photoluminescence of MAPbI$_3$ thin film with excitation powerat30 µW. When the temperature was decreased from room temperature to 5 K, significant increase in PL intensity is observed. Spectra peak shifts and variation in spectra shape were also observed with decreasing temperature. Figure 4.10 a) shows the contour map representation of the temperature dependence of luminescence spectra obtained under pulsed laser power density of 0.43 µJ/cm^2 (30 µW) at the same position on the thin film sample. Various interesting features are observed as the temperature is reduced. For instance, when the temperature was decreased to approximately 170 K, the RT PL spectra around 780 nm red-shifted by about 18 nm, and the full-width at half maximum (FWHM) narrowed from 53 nm to 32 nm. The typical luminescence spectra are shown in Figure1 b). The red-shift of the PL peaks is attributed to the temperature dependence of the energy bandgap (E_g), namely that E_g decreases with decreasing temperature. Presently, it is unclear whether the photoexcited species at room temperature exist as excitons or free carriers. This uncertainty stems from the reported low exciton binding energies (E_b) of this material which ranges from 19 to 50 meV, comparable to RT thermal energies of $k_\beta T$ ~25 meV [3,33-36].The observed spectral narrowing with temperature decrease for the 293 – 170 K interval is in agreement with the regular behaviour presented by semiconductor materials free of confinement potential fluctuations[37].

Furthermore, a decrease in temperature from 170 to 150Kshowed continued red-shift of the main peak and the appearance of a new band at~746 nm. These peaks are labeled as L (lower energy) and H (higher energy) respectively for easy referencing. The observed features in the 150 – 170 K interval are attributed mainly to a structural phase transition of the hybrid perovskite, notably from a tetragonal to an orthorhombic structure, the transition temperature of which is measured to be ~162 K in agreement with earlier publications [38]. Also, below the phase transition temperature, new exciton transition appears. When the temperature is further reduced, the H peak showed gradual red-shift and increase in PL intensity while the L peak showed reduction in red-shift as the temperature decreases to ~100 K. Upon further decrease in temperature below ~100 K, both peaks show gradual red-shift with the H peak dominating the spectrum until at 5 K where the L peak disappeared. At this temperature, the H peak is centered at ~780 nm, exhibiting the characteristic behaviour of the RT PL spectra. The PL spectra of the L peak presented an asymmetric behaviour predominantly in the 75 - 50 K interval with a long shoulder that extended to 900 nm. This behaviour can be associated with trap-related recombination or the presence of triplet states. However, the PL spectra of the H peak presented a symmetric behavior that is characteristic of delocalized excitons.
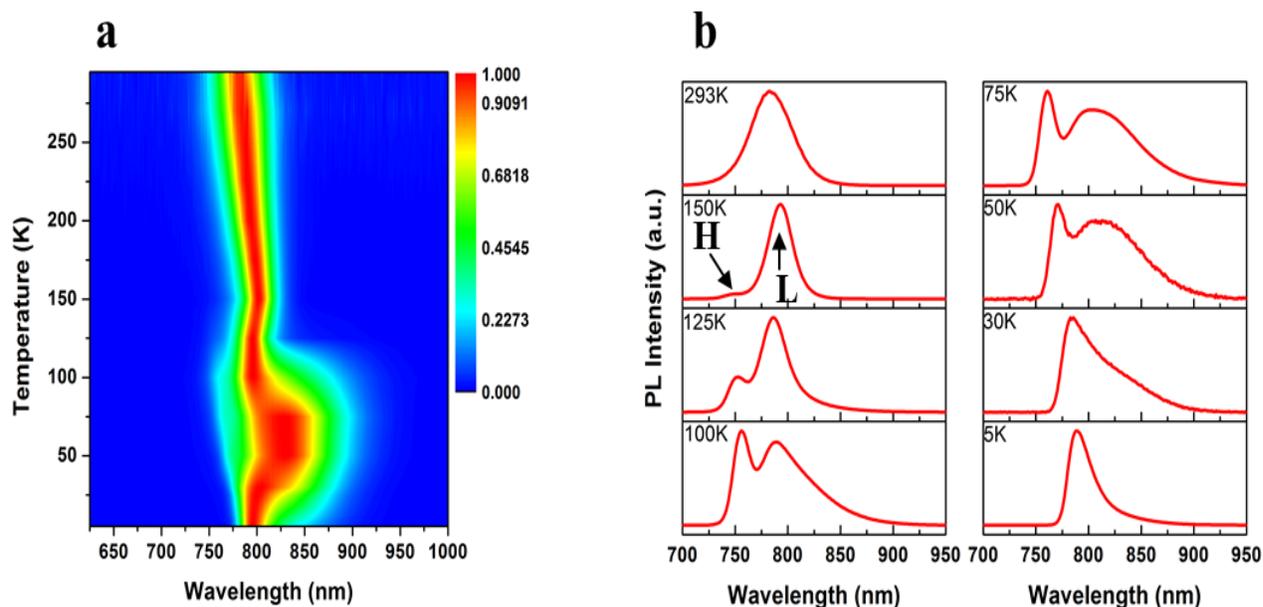
Figure 4.10. Temperature dependent steady state photoluminescence (PL) of MAPbI$_3$ thin film. (a) Temperature dependent PL map from solution-processed MAPbI$_3$ thin film. (**b**) Corresponding temperature dependent PL spectrum taken under laser excitation density of 0.43μJ/cm^2.

The power-dependent steady state PL spectra normalized with respect to the maximum peak is shown in Figure 4.11. The sample was excited with a 400 nm pulsed laser and the excitation power was varied from 1 to 400 μW. In the 293 - 150 K interval, the PL spectra showed no excitation power dependence. However, decreasing the temperature below 150 K, the power dependence steadily increased significantly till around 50 K and then gradually reduced as the temperature approached 5 K. Although the H peak showed excitation power dependence of the PL intensity, its peak energies are independent in the 150 – 50 K interval. Similarly, the main peak and subsequently, the L peak exhibited no dependence of its peak energy on excitation power from RT to about 125 K. However, the strong power dependence with notable blue-shift in the peak energy of the L peaks and the reduction in linewidth and intensity with increasing power occurred during the decrease in temperature from 125 to 30 K. As already observed in the temperature dependent PL spectra, from 30 to 5 K, the L peak steadily disappeared but with significant blue-shift in peak energies with increasing excitation power. The FWHM also decreased substantially with increasing power as temperature is reduced from 50 K to 5 K.
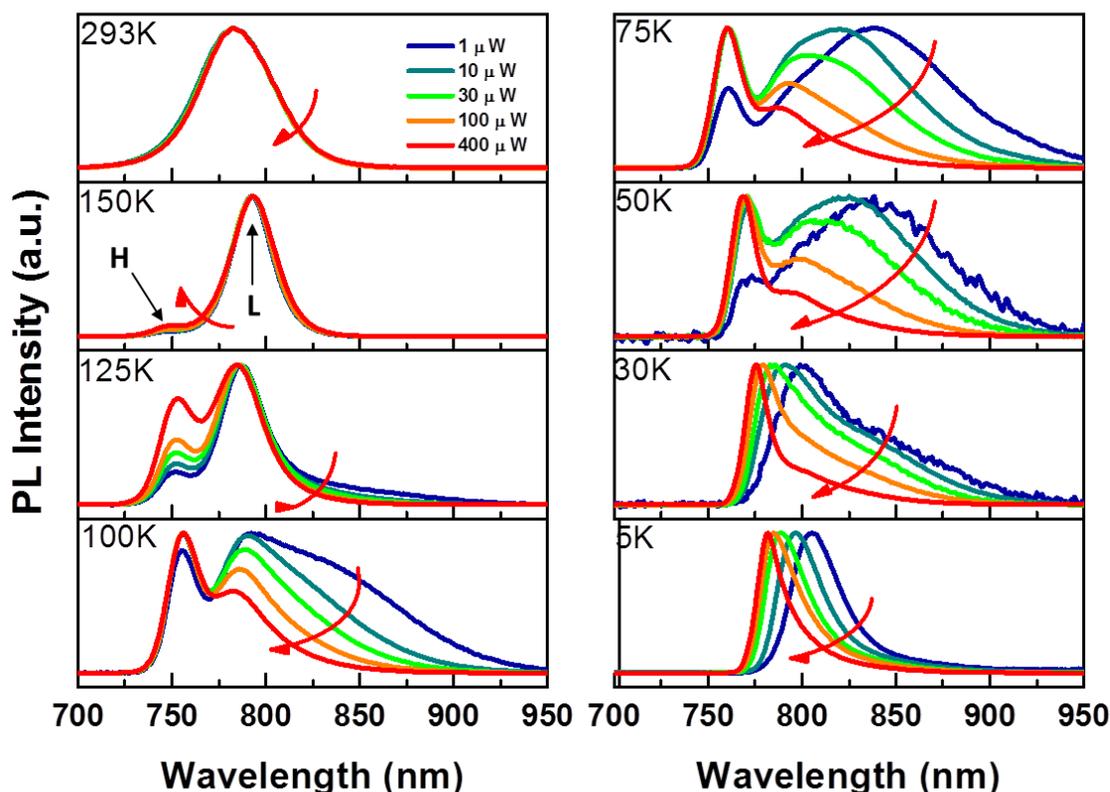
Figure 4.11.Power-dependent photoluminescence (PL) of thin film. PL of $CH_3NH_3PbI_3$is strongly dependent on the excitation power, especially below 150 K. The laser power is varied from 1 µW (~ 14 nJ/cm^2) to 400 µW (~ 5.68 µJ/cm^2).

4.3.3   Temperature and power dependent time-resolved photoluminescence

To unravel the dynamics of emission processes, temperature dependent transient PL measurements were taken following femto-second pulsed photoexcitations. Figure 4.12 a) shows the streak camera imaging from room temperature to 5 K with 400 nm excitation pulses at constant excitation power of 100 µW. At room temperature, the emission spectrum is invariant with time, highlighting the low degree of disorder present in the thin film. The transient PL spectra exhibits different characteristic behaviour below 150K.At 130 K, a new fast decay channel in the 730 – 755 nm range is observed consistent with the steady state PL measurement. This channel is labeled M and the main peak or channel is labeled N in Figure 4.12 a).The emission decay is of the order of 1 ns for the M peak, much faster than the emission of the N peak and is attributed to radiative decay of the free excitons. It is observed to rapidly red-shift as the temperature decreases further. On the other hand, the N peak exhibits an extremely long-lived exciton

emission with lifetime of several microseconds. Comparing this observation with the steady state PL measurement reveals that almost all the integrated intensities are due to the slow exponential component (N peak) of the spectra. The decrease in the lifetime of the fast emission component and the increase for the long-lived charge carrier emission is revealed when the temperature was steadily decreased. This is shown in Figure 4.12 b) for temperatures at 5, 100 and 293 K. At room temperature (293K), the PL decay is mono-exponential and becomes bi-exponential at lower temperatures below 150 K where the short lifetime and long-lived charge carriers are observed. The emission decays at 100 K demonstrate the co-existence of short lifetime and long-lived excitons.
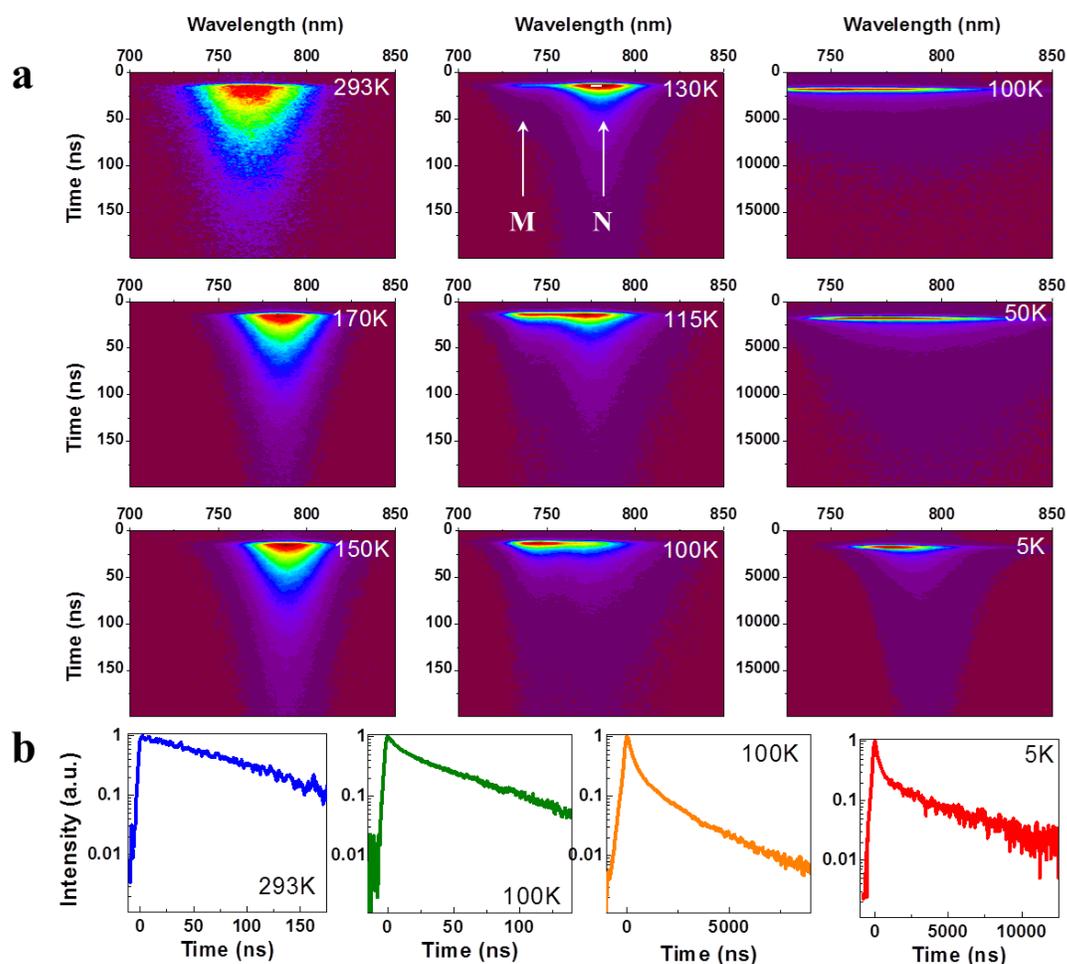

Figure 4.12.Time-resolved photoluminescence (PL) emission from 293 K to 5K. (a) Streak camera image showing the time-resolved emission of the PL peaks at different temperatures. (b) Normalized transient PL decay dynamics at three different temperatures.
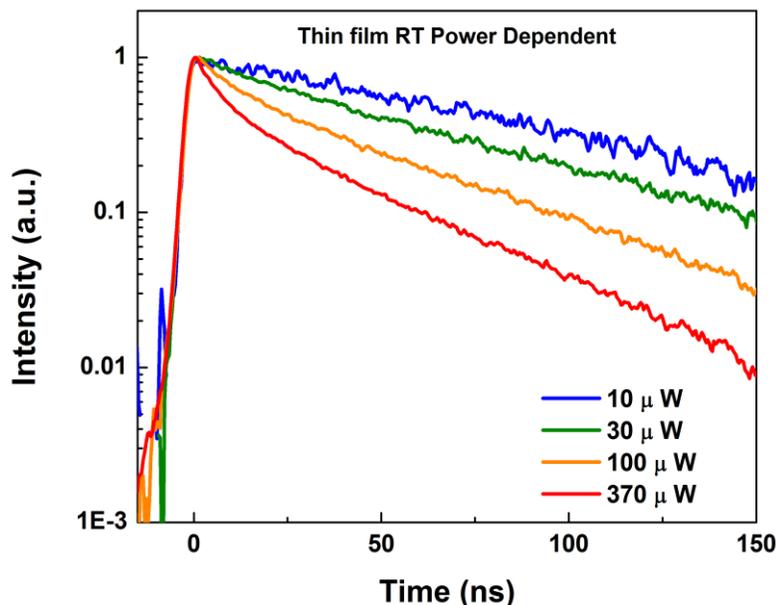
Figure 4.13. Transient PL decay (normalized) of $CH_3NH_3PbI_3$ thin film at room temperature with pump power ranging from 10 to 370 µW.

Table 4.1. Best-fit parameters of time-resolved photoluminescence of the thin film at room temperature with function $I = \sum_i A_i \exp(-t/\tau_i)$.

Power (µW)	Lifetime (ns)	
	τ_1	τ_2
10	83.7 (100%)	-
30	66 (80%)	9.3 (20%)
100	49.5 (56.9%)	7.5 (43.1%)
370	37.2 (39.7%)	5.3 (60.3%)

To elucidate the effects of laser power on the decay lifetimes, power-dependent time-resolved PL measurements were carried out with excitation power from 10 to 400 µW. At room temperature, a fast initial decay component becomes increasingly significant with increasing excitation fluence. The power dependent transient PL measurement at room temperature is shown in Figure 4.13. From the PL at ultra-low excitation fluence (10 µW, 1.5×10^{16} cm^{-3}), a monomolecular recombination lifetime of 83 ns is extracted by fitting a single exponential decay function to the data. This dynamics reflects intrinsic charge carrier decay lifetime. The figure also demonstrates that the shapes of the emission spectra are independent of excitation power. This suggests high crystalline quality and absence of disorder-related

effects at room temperature. At elevated charge carrier densities (high pump power), it can be observed from the multi-exponential characteristics of the decay curve that higher order effects such as bimolecular and Auger recombination processes increasingly play a role. The highest laser power applied is 400 µW, corresponding to an absorbed peak photon density of 6×10^{17} cm^{-3}. To evaluate the recombination lifetimes, the measurements at room temperature were fitted with bi-exponential decay function given by $I = \sum_i A_i \exp(-t/\tau_i)$. The overall emission shows a much faster decay with the appearance of a second shorter lifetime at higher pump power. This is consistent with the opening up of the additional relaxation pathways observed, corresponding to an increase in charge carrier interactions. The best-fit lifetime parameters of the power dependent transient PL measurements at room temperature are tabulated in Table 4.1 showing the increasing recombination effects with increasing pump power. Regarding the higher order effects, Wehrenfenning *et al.* demonstrated that the bimolecular recombination rate in this material is extremely low, defying the Langevin recombination limit by at least four orders of magnitude [39]. This explains the long recombination lifetime measured and the long charge carrier diffusion lengths reported for this material [23, 24].
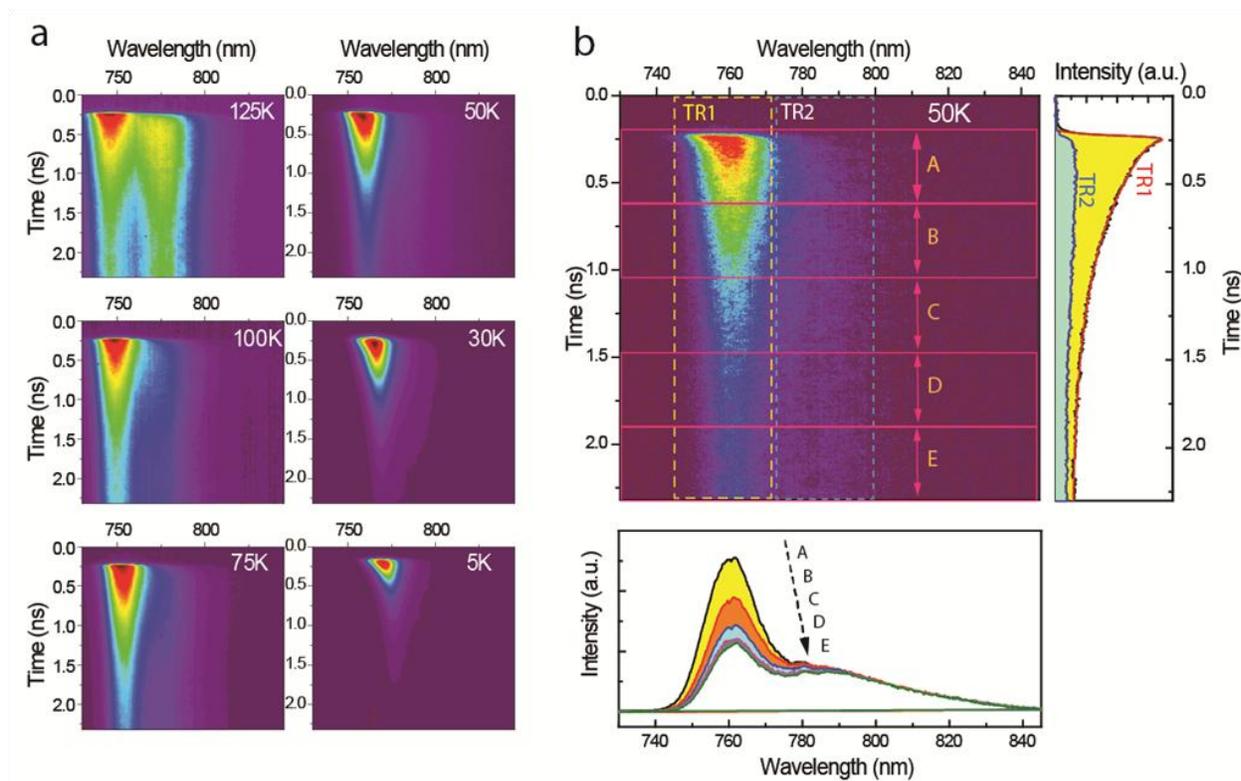

Figure 4.14. Time-resolved fast decay components at low temperature. (a) Streak camera image with time-window of 2.25 ns showing the decay of short lifetime exciton. The images were taken under laser excitation density of 5.86 µJ/cm^2. (b) Streak camera image of emission at 50 K taken under laser excitation density of 1.42 µJ/cm^2.

As mentioned above, the dynamics at low temperature is much more complex. The emission dynamics show multi-components: the appearance of the new fast emission band (M peak) and the long-lived tail (N peak). To elucidate the fast emission components, the initial decay processes within the first 2 ns time-window at low temperatures were measured as presented in Figure 4.14.The streak camera images show that in the 5 -125 K interval, the recombination rate of the fast emission component increases as temperature decreases (Figure 4.14 a)). In Figure 4.14 b), the characteristics of the emission at 50 K for different sub-time windows (bottom-plot) and also, the lifetimes at two different wavelength channels, TR1 and TR2 corresponding to the main peak and its shoulder (right-plot) respectively are illustrated. The bottom-plot shows invariant characteristic behaviour of the emission spectra at the different time windows for the different wavelength channels. However, the right-plot shows very fast radiative and extremely slow emission decay for the TR1 and TR2 respectively.

Figure 4.15 shows the power dependent transient PL measurements taken at 5 and 50 K. The measurements reveal strong power dependence of the long-lived states whereas the fast decay components are weakly dependent. The measurements exhibit multi-exponential decay transient, highlighting the presence of multi-processes or higher order effects occurring at these temperatures. The slow decay process regions are fitted with mono-exponential decay function while the fast decay process regions are fitted with bi-exponential decay function. At 50 K, the recombination lifetime for the slow processes increased from 2.51 to 6.96 µs when the pump power was decreased from 28.9 to 2.89 pJ. The fast decay is clearly resolved in Figure 4.15 b) and the lifetime is extracted: $\tau_1 = 0.42\ ns$, $\tau_2 = 14.5\ ns$ for pump power at 28.9 pJ.However, compared to the recombination processes at 50 K, the processes at 5 K do not show very strong dependence on pump power. For instance, for the slow processes, the lifetime varied by ~ 1 µs when the pump power was decreased from 28.9 to 2.89 pJ. We observed that at pump power of 28.9 pJ, the lifetime at 5 K (3396 ns) is longer than at 50 K (2510 ns). However, the lifetime for the fast decay shown in Figure 4.15 d) is much shorter: $\tau_1 = 0.15\ ns$, $\tau_2 = 0.73\ ns$.The various recombination processes occurring for the fast decay can be attributed to interactions involving excitons, bi-excitons and trions while the slow decay processes are indicative of defect and triplet states.
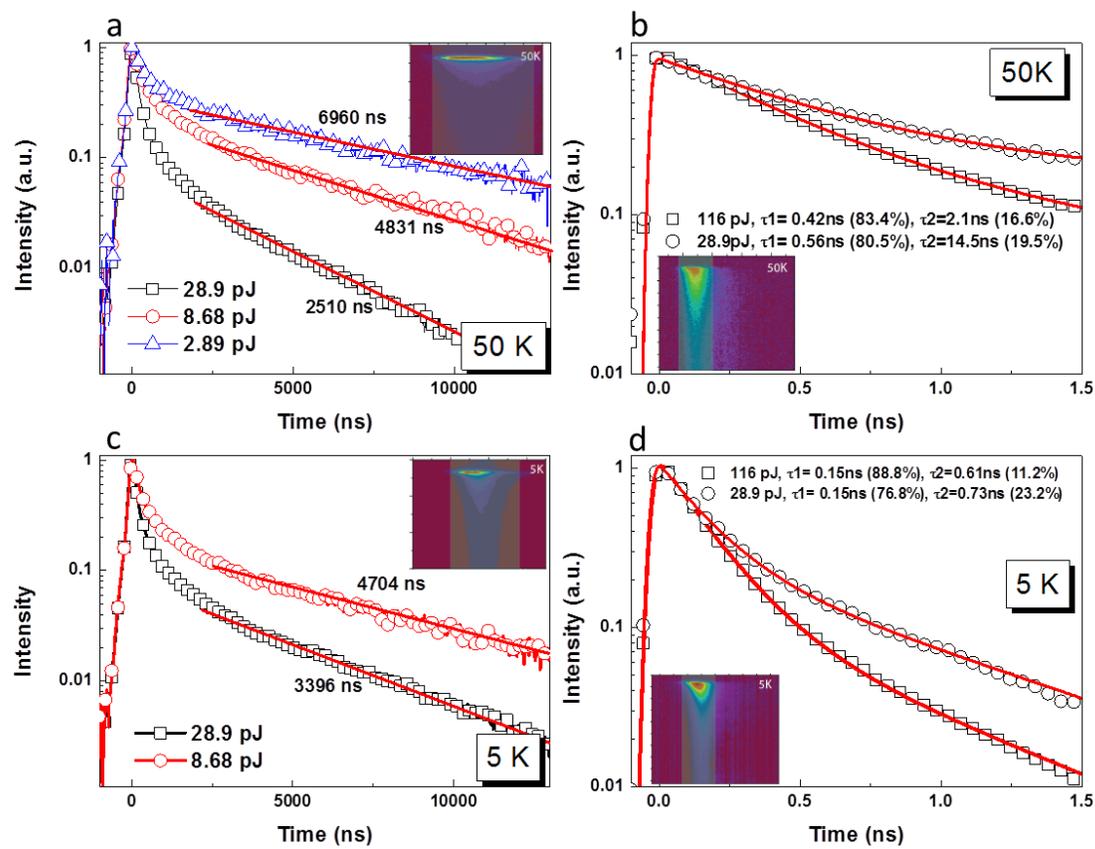
Figure 4.15. (**a, b**) Power dependent time-resolved PL measurements taken at 50 K. (**c, d**) Power dependent time-resolved PL measurements taken at 5 K. Inset indicates the positions where the time-resolved PL dynamics were extracted.

CHAPTER 5

SUMMARY

The surge in perovskite solar cell efficiency from 3.8 % to 19.3% over a four year period has opened up several pressing questions and created gaps between their skyrocketing efficiency and the understanding of their materials properties and working principles. With on-going efficiency improvements expected, much is required in understanding their materials properties and optimal cell designs. Thus, for any given material system, factors such as device processing and the ensuing morphology and coverage strongly affect the carrier dynamics and the device performance. Hence, the focus of this study has been on growth techniques that ensures homogeneity and continuity of perovskite thin films by optimizing and characterizing model $MAPbI_3$ thin film. Photophysical investigation of the nature of the fundamental photoexcitations to understand their intrinsic properties were also explored.

Two deposition methods were used in the morphology optimization processes: single-step precursor and the inter-diffusion reaction deposition techniques based on spin-coating and blade coating methods. The perovskite $MAPbI_3$ thin films are successfully synthesized without impurities as examined by absorption and powder X-ray diffraction analysis reported. While low temperature spin coating is among the simplest methods to fabricate low-cost solar cell devices, it is found to be very challenging to grow homogeneous and continuous perovskite thin films by directly depositing single precursor solution of mixed MAI and PbI_2 precursors from DMF or GBL either on ITO or AZO. The thin films made from equimolar solution of MAI and PbI_2 precursors formed domains with fiber-like crystallites which are randomly distributed and highly non-continuous and inhomogeneous on the ITO substrate. The deposited 3:1 ($MAI:PbI_2$) mole ratio films showed no clear domains and the fiber structures were eliminated with fewer pores on the ITO. The deposition from DMF showed significant decrease in grain size and improved morphology compared to deposition from GBL. There is no significant difference in the quality of the films deposited on both ITO and AZO using the 3:1 ($MAI: PbI_2$) mole ratio precursor solution. On the other hand, the inter-diffusion reaction method shows a very significant improvement in the film quality but not perfectly homogeneous. The low homogeneity is mainly due to the non-uniform PbI_2 film deposited by spin coating. Morphology optimization based on doctor blading however, gave a relatively good control of the film uniformity and reproducibility. The quality of the films showed strong dependence on solution temperature, pre-heated substrate temperature, annealing temperature and time and blading speed. Although the optimal films deposited by single-step precursor deposition method on ITO or AZO were non-continuous but relatively uniform, film formation by inter-diffusion reaction

method were highly controlled to form uniform thin films of ~ 300 nm roughness. The quality of the PbI_2-coated films is observed to affect the roughness of the perovskite thin film. The optimal $MAPbI_3$ film produced has thickness of ~ 790 nm of which the PbI_2 film is ~ 300 nm thick. The quality of the films formed is still opened for improvement.

The perovskite film morphology dependence was tested by fabricating devices which showed less than 1% efficiency. This poor performance is attributed to a number of factors including poor electron or hole selective contact materials used in the fabrication, unclean glove-box atmosphere, the need for a mesoporous electron selective contact layer or hole blocking layer. These factors need further investigation to gain deeper insight of the poor device performance.

The PL spectra of the $MAPbI_3$ showed strong temperature dependence with intriguing features. Besides the red-shift of the room temperature emission peak at ~ 780 nm with decreasing temperature, which is characteristic of the temperature dependence of the energy bandgap, two emission peaks are observed at ~ 745 nm and ~ 795 nm below 150 K. These emission peaks persist until 30 K where only one peak is observed at ~ 780 nm. The observed change in the PL spectra is accompanied by a structural phase transition from tetragonal to orthorhombic phase at ~ 162 K. The excitation power dependent PL spectra show no effect at room temperature. However, below 125 K, an unusual blue-shift in the PL spectra with increasing power intensity is observed. Transient PL measurements at different temperatures show an extreme increase in the decay time from ~ 83.7 ns at 293 K to 6960 ns at 50 K. The power dependent time-resolved PL measurements show a decrease in recombination lifetime and a transition from a mono-exponential decay to a multi-exponential decay when the excitation power is increased. The PL decay at 293 K shows a mono-exponential decay with time constant of ~ 83.7 ns when excited at the power of 10 µW while at excitation power of 370 µW, it shows a faster component of ~ 5.3 ns (60.3%) and a slower component of 37.2 ns (39.7%).

REFERENCES

1. M. A. Green, K. Emery, Y. Hishikawa, W. Warta, E. D. Dunlop, Solar Cell Efficiency Tables (Version 40), *Prog. Photovoltaics* **20**, 606 (2012).

2. M. M. Lee, J. Teuscher, T. Miyasaka, T. N. Murakami, H. J. Snaith, Efficient Hybrid Solar Cells Based on Meso-Superstructured Organometal Halide Perovskites, *Science* **338**, 643 (2012).

3. A. Kojima, K. Teshima, Y. Shirai, T. Miyasaka, Organometal Halide Perovskites as Visible-Light Sensitizers for Photovoltaic Cells, *J. Am. Chem. Soc.* **131**, 6050 (2009).

4. H. S. Kim, C. R. Lee, J. H. Im, K. B. Lee, T. Moehl, A. Marchioro, S. J. Moon, R. Humphrey-Baker, J. H. Yum, J. E. Moser, M. Grätzel, N. G. Park, Lead Iodide Perovskite Sensitized All-Solid-State Submicron Thin Film Mesoscopic Solar Cell with Efficiency Exceeding 9%, *Sci. Rep.* **2**, 591 (2012).

5. J. H. Noh, S. H. Im, J. H. Heo, T. N. Mandal, S. I. Seok, Chemical Management for Colorful, Efficient, and Stable Inorganic-Organic hybrid Nanostructured solar cells, *NanoLett.* **13**, 1764 (2013).

6. J. M. Ball, M. M. Lee, A. Hey, H. J. Snaith, Low-Temperature Processed Meso-superstructured to Thin-film Perovskite Solar Cells, *Energy Environ. Sci.* **6**, 1739 (2013).

7. D. Liu, T. L. Kelly, Perovskite Solar Cells with a Planar Heterojunction Structure Prepared Using Room-temperature Solution Processing Techniques, *Nature Photonics* **8**, 133 (2013).

8. J. H. Im, C.R. Lee, J. W. Park, N. G Park, 6.5% Efficient Quantum-Dot-Sensitized Solar Cell, *Nanoscale* **3**, 4088 (2011).

9. L. Etgar, P. Gao, Z. Xue, Q. Peng, A. K. Chandiran, B. Liu, Md. K. Nazeeruddin, M. Grätzel, Mesoscopic $CH_3NH_3PbI_3/TiO_2$ Heterojunction Solar Cells, *J. Am. Chem. Soc.* **134**, 17396 (2012).

10. H. J. Snaith, Perovskites: The emergence of a New Era for Low-Cost, High-Efficiency Solar Cells, *J. Phys. Chem. Lett.* **4**, 3623 (2013).

11. D.B. Mitzi, Progress Inorganic Chemistry; K. D. Karlin, Ed.; Wiley-Interscience: New York, **43**, 1-121 (1999).

12. A. O. Polyakov, A. H. Arkenbout, J. Baas, G. R. Blake, A. Meetsma, A. Caretta, P. H. M. van Loosdrecht, **and** Thomas T. M. Palstra, Coexisting Ferromagnetic and Ferroelectric Order in a $CuCl_4$-based Organic–Inorganic Hybrid, *Chem, Mater.* 24, 133 (2012).

13. G. Hodes, Perovskite-Based Solar Cells, *Science* **342**, 317 (2013).

14. B. O'Regan, M. Grätzel, A Lost-Cost, High-Efficiency Solar Cell Based on Dye-Sensitized Colloidal TiO_2 Films, *Nature*, **353**, 737 (1991).

15. J. H. Heo, S. H. Im, J. H. Noh, T. N. Mandal, C-S. Lim, J. A. Hang, Y. H. Lee, H-j. Kim, A.

Sarkar, M. K. Nazeeruddin, M. Grätzel& S. Il Seok, Efficient Inorganic-Organic Hybrid Heterojunction Solar Cells Containing Perovskite Compound and Polymeric Hole Conductors, *Nature Photonics* **7**, 486 (2013).

16. M. A. Loi, J.C. Hummelen, Hybrid Solar Cells, *Nature Materials* **12**, 1087 (2013).

17. J. Burschka, N. Pellet, S. J. Moon, R. Humphry-Baker, P. Gao, M. K. Nazeeruddin, and M. Gratzel, *Nature,***499**, 316 (2013).

18. M. Liu, M. B. Johnston and H. J. Snaith, *Nature*, **501**, 395 (2013).

19. J. T. Wang, J. M. Ball, E. M. Barea, A. Abate, J. A. Alexander-Webber, J. Huang, M. Saliba, I. Mora-Sero, J. Bisquert, H. J. Snaith and R. J. Nicholas, *NanoLett*., **14**, 724 (2014).

20. K. Wojciechowski, M. Saliba, T. Leijtens, A. Abate and H. J. Snaith, *Energy Environ. Sci*., **7**, 1142 (2014).

21. http://www.nrel.gov/ncpv/images/efficiency_chart.jpg, The National Renewable Energy Laboratory (NREL) 2013.

22. R. F. Service, Perovskite solar cells keep on surging, *Science* 344, 458 (2014).

23. S.D. Stranks, G. E. Eperon, G. Grancini, C. Menelaou, M. Alcocer, T. Leijtens, L. M. Herz, A. Petrozza, H. J. Snaith, Electron-Hole Diffusion Lengths Exceeding 1 Micron in an Organometal Trihalide Perovskite Absorber, *Science*, **342**, 341 (2013).

24. G. Xing, N. Mathews, S. Sun, S. S. Lim, Y. M. Lam, M. Grätzel, S. Mhaisalkar, T. C. Sum, Long-Range Balanced Electron- and Hole-Transport Lengths in Organic-Inorganic $CH_3NH_3PbI_3$, *Science*, **342**, 344 (2013).

25. S. M. Sze, K. K. Ng, Physics of Semiconductor Devices; John Wiley & Sons (2007).

26. H. Hoppe and N. S. Sariftci, Crystalline Properties of Laser Crystallized Silicon Films, *J. Mater. Res*., **19**, 7, 1924 (2004).

27. D. V. Talapin, J. S. Lee, M. V. Kovalenko and E. V. Shevchenko, Prospects of Colloidal Nanocrystals for Electronic and Optoelectronic Applications, *Chem. Rev*., **100**, 428 (2010).

28. I. Reidel, J. Parisi, V. Dyakonov, L. Lutsen, D. Vanderzande and J. C. Hummelen, Effect of Temperature and Illumination on Electrical Characteristics of Polymer-Fullerene Bulk-Heterojunction Solar Cells, *Adv. Funct. Mater*., **15**, 58 (2004).

29. K. Sugiyama, H. Ishii, Y. Ouchi and K. Seki, Dependence of Indium–Tin–Oxide Work Function on Surface Cleaning Method as Studied by Ultraviolet and X-ray Photoemission Spectroscopies, *J. Appl. Phys.* **87**, 295 (2000).

30. T.Stubhan,H. Oh, L. Pinna, J. Krantz, I.Litzov and C. J. Brabec, Inverted Organic Solar Cells Using a Solution Processed Aluminum-doped Zinc Oxide Buffer Layer, *Organic Electronics* **12** 1539 (2011).

31. Q. Chen, H. Zhou, Z. Hong, S. Luo, H. S. Duan, H. H. Wang, Y. Liu, G. Li and Y. Yang, *J. Am. Chem. Soc.*, **136**, 622 (2014).

32. G. E. Eperon, V. M. Burlakov, P. Docampo, A. Goriely, and H. J. Snaith, Morphological Control for High Performance, Solution-Processed Planar Heterojunction Perovskite Solar Cells, *Adv. Funct. Mater.* **501**, 195 (2013).

33. S. Sun, T. Salim, N. Mathews, M. Duchamp, C. Boothroyd, G. Xing, T. C. Sum and Y. M. Lam, *Energy Environ. Sci.*, **7**, 399 (2014).

34. M. Hirasawa, T. Ishihara, T. Goto, K. Uchida and N. Miura, *Phys. B*, **201**, 427 (1994).

35. T. Ishihara, J. Lumin., **60-61**, 269 (1994).

36. K. Tanaka, T. Takahashi, T. Ban, T. Kondo, K. Uchida and N. Miura, Solid State Commun., 127, 619 (2003).

37. S. A. Lourenc¸o, I. F. L. Dias, J. L. Duarte, E. Laureto, D. O. Toginho Filho, E. A. Meneses, and J. R. Leite, *Eur. Phys. J.* **B 21**, 11 (2001).

38. N. Onoda-Yamamuro, T. Matsuo, and H. Suga, Calorimetric and IR spectroscopic studies of phase transitions in methylammonium trihalogenoplumbates (II), *Journal of Physics and Chemistry of Solids*, v. 51,**12**, 1383 (1990).

39. C. Wehrenfennig, G. E. Eperon, M. B. Johnston, H. J. Snaith, and L. M. Herz, High Charge Carrier Mobility's and Lifetimes in Organolead Trihalide Perovskites, *Adv. Mater.*, **26**, 1584 (2014).